
Electronic Thesis and Dissertation Repository

10-5-2022 10:30 AM

Technical Adaptations for Cardiac Sodium MRI

Taylor L. Marcus, *The University of Western Ontario*

Supervisor: McIntyre, Christopher, *The University of Western Ontario*

A thesis submitted in partial fulfillment of the requirements for the Master of Science degree in Medical Biophysics

© Taylor L. Marcus 2022

Follow this and additional works at: <https://ir.lib.uwo.ca/etd>



Part of the [Cardiovascular Diseases Commons](#), [Medical Biophysics Commons](#), [Nephrology Commons](#), [Pathological Conditions, Signs and Symptoms Commons](#), and the [Radiology Commons](#)

Recommended Citation

Marcus, Taylor L., "Technical Adaptations for Cardiac Sodium MRI" (2022). *Electronic Thesis and Dissertation Repository*. 8902.

<https://ir.lib.uwo.ca/etd/8902>

This Dissertation/Thesis is brought to you for free and open access by Scholarship@Western. It has been accepted for inclusion in Electronic Thesis and Dissertation Repository by an authorized administrator of Scholarship@Western. For more information, please contact wlsadmin@uwo.ca.

Abstract

Cardiac sodium (Na^+) MRI has the potential to unveil relationships between chronic kidney disease (CKD) and cardiovascular disease (CVD). Unfortunately, this modality requires many technical adaptations before it's possible to extract and compare image data between individuals. This study investigated whether cardiac electrocardiogram (ECG) gating could improve image quality, and whether a uniform phantom could increase signal uniformity if a surface coil is used to acquire the image. Healthy participants were imaged with a custom-built surface coil and 3.0-T MR system. Cardiac gated images presented with a decreased signal-to-noise ratio (SNR), but intensity correction significantly increased image signal uniformity. Future studies using cardiac Na^+ MRI with a surface coil should consider implementing signal intensity correction but should recognize that cardiac gating reduces image quality unless scan time is increased.

Keywords

Cardiac Sodium MRI, Cardiac Magnetic Resonance, ECG Gating, Intensity Correction, Surface Coil, Chronic Kidney Disease (CKD), Hemodialysis (HD)

Summary for Lay Audience

Introduction: Patients with damaged kidneys are also often found to suffer from heart conditions. Since damaged kidneys can't adequately excrete excess sodium in the body, it would be beneficial to image sodium in the heart tissue of kidney disease patients and compare this to their heart function. This can be done using sodium MRI, but the low concentration of sodium in tissue is a challenging problem and imaging hardware and techniques must first be optimized. In this study, we set out to improve sodium MR image quality by removing the motion of the heart during imaging and correcting for the non-uniform image signal created by the custom-made imaging hardware.

Methods: We imaged the hearts of four healthy individuals with sodium MRI in each part of this study. In the first part of this study, each participant's heart was imaged with and without heart motion. These images were then compared to assess image quality. In the second part of the study, a large bin with vials containing different concentrations of saline solution were imaged, along with large bin of uniform saline concentration. The image of the vials was divided by the image of the bin to correct for the signal intensity uniformity. Vial images before and after correction were compared to determine whether the intensity was corrected. This correction was then applied to each participant's heart images as well.

Results: Removing heart motion during sodium imaging was not found to increase image quality but correcting the signal intensity uniformity of the images was found to be possible.

Conclusions: Technical adaptations must be implemented when imaging human hearts with sodium MRI. Removing heart motion is not necessary for quality images. However, signal intensity correction is necessary if quantitative measurements from image data are to be extracted and compared between participants. Dividing a heart sodium image by an image of a uniform saline solution can correct for the inherent signal intensity non-uniformity. Future studies may include using these technical adaptations to image the hearts of patients with kidney disease with sodium MRI to determine whether sodium build-up in heart tissue correlates with heart complications.

Acknowledgments

I would first like to acknowledge that this research was conducted on the traditional territories of the Anishinaabek (Ah-nish-in-a-bek), Haudenosaunee (Ho-den-no-show-nee), Lūnaapéewak (Len-ahpay-wuk) and Chonnonton (Chun-ongk-ton) Nations, on lands connected with the London Township and Sombra Treaties of 1796 and the Dish with One Spoon Covenant Wampum. I would also like to acknowledge the Indigenous Student Centre at Western University for providing me with the opportunity to find my Indigenous identity through their Head & Heart program, and for the financial support they gave me through the Indigenous Graduate Student Research Award. As an Indigenous researcher, I feel it is important to acknowledge all of the relationships that have helped me through the past two years of my Master's degree, whether academically or personally.

I would like to thank the Medical Biophysics program at Western University for the breadth of knowledge they have provided me throughout the past six years. Specifically, I would like to thank Dr. Timothy Scholl for being a phenomenal advisor and supporter, Dr. Alireza Akbari for his constant mentorship and MRI expertise, and my supervisor Dr. Christopher McIntyre for his clinical insight and simply taking the time out of his busy schedule for his students – the amount of work he has taken on amazes me. I would like to thank David Reese for his MRI technologist work, Josephine Tan for her knowledge on image processing and data analysis, and all the individuals that volunteered to be imaged. I would also like to thank Western University for supporting me financially throughout my degree with the Western Graduate Research Scholarship and providing me with the opportunity to receive an Ontario Graduate Scholarship.

Completing my degree amid the COVID-19 pandemic has been extremely difficult, and I could not have done it without the support of my parents Tracy and Brian, my brother Spencer, and my partner Brandon. These past two years have been filled with some of the highest of highs but also the lowest of lows, and I appreciate everyone that has continued to support me throughout this convoluted journey.

Table of Contents

Abstract.....	ii
Summary for Lay Audience.....	iii
Acknowledgments.....	iv
Table of Contents.....	v
List of Tables.....	ix
List of Figures.....	x
List of Abbreviations.....	xiv
Chapter 1.....	1
1 Introduction.....	1
1.1 Motivation and Overview.....	1
1.2 The Kidney.....	2
1.2.1 Kidney Anatomy.....	2
1.2.2 Kidney Physiology.....	4
1.2.3 Sodium (Na ⁺) Handling by the Kidney.....	5
1.2.4 Chronic Kidney Disease (CKD).....	6
1.3 The Heart.....	9
1.3.1 Cardiac Anatomy.....	9
1.3.2 Cardiac Physiology.....	10
1.3.3 Cardiovascular Disease (CVD) in CKD Patients.....	15
1.4 Biological Sodium (Na ⁺).....	18
1.4.1 Fluid Compartments.....	18
1.4.2 The Role of Sodium (Na ⁺) in the Body.....	19
1.4.3 Osmotically Inactive Sodium (Na ⁺).....	20
1.4.4 Sodium (Na ⁺) in CKD.....	21

1.4.5	Sodium and Cardiac Injury	22
1.5	Magnetic Resonance Imaging (MRI).....	25
1.5.1	Pulse Sequences	27
1.5.2	Proton (H^+) MRI	28
1.5.3	Sodium (Na^+) MRI.....	31
1.5.4	Radiofrequency (RF) Coils	33
1.6	Objectives and Hypotheses	34
Chapter 2	35
2	The Effects of ECG Gating on Na^+ MR Image Quality.....	35
2.1	Introduction.....	35
2.1.1	Sodium (Na^+) in the Body.....	35
2.1.2	Sodium (Na^+) MR Imaging & Applications	35
2.1.3	Challenges of Cardiac Sodium (Na^+) MRI	36
2.1.4	Cardiac Sodium (Na^+) MR ECG Gating.....	36
2.1.5	Objective and Hypothesis	37
2.2	Methodology	38
2.2.1	Study Design.....	38
2.2.2	Participants.....	38
2.2.3	H^+ and Na^+ MR Acquisition	38
2.2.4	Data Analysis	39
2.3	Results.....	43
2.3.1	Measuring the Point Spread Function (PSF)	44
2.3.2	Measuring the Signal-to-Noise Ratio (SNR)	45
2.3.3	Measuring the Geometrical Distortion.....	46
2.4	Discussion	48
Chapter 3	51

3	Intensity Correction for Cardiac Na ⁺ -MR Images Acquired with a Surface Coil	51
3.1	Introduction.....	51
3.1.1	Sodium (Na ⁺) in the Body.....	51
3.1.2	Sodium (Na ⁺) MRI.....	51
3.1.3	Sodium (Na ⁺) in Kidney Disease	52
3.1.4	Challenges of Sodium (Na ⁺) MRI.....	52
3.1.5	Surface Coils.....	52
3.1.6	Intensity Correction of Surface Coil Images	53
3.2	Methodology	54
3.2.1	Study Design.....	54
3.2.2	Participants.....	55
3.2.3	Sensitivity Correction Phantom MR Acquisition	55
3.2.4	Calibration Vials MR Acquisition	56
3.2.5	Cardiac MR Acquisition	57
3.2.6	Image Processing	58
3.2.7	Image Analysis.....	60
3.2.8	Statistical Analysis.....	60
3.3	Results.....	60
3.3.1	Calibration Scans	60
3.3.2	Cardiac Scans.....	63
3.3.3	Interobserver and Interscan Variability	65
3.4	Discussion.....	66
	Chapter 4.....	70
4	Conclusions and Future Work.....	70
4.1	Discussions and Conclusions	70
4.2	Challenges and Limitations.....	72

4.2.1	COVID-19 Pandemic.....	72
4.2.2	Limitations of Na ⁺ MRI.....	72
4.2.3	Sodium Quantification.....	73
4.2.4	Application to Future Work.....	73
4.3	Future Work.....	74
	References.....	76
	Curriculum Vitae.....	84

List of Tables

Table 1.1: The Five Stages of CKD with eGFR Values	7
Table 1.2: Parameters for Assessing Cardiac Function	30
Table 2.1: Septum thickness means and ranges measured from each participant's Na ⁺ MR images in two separate septum locations. Means include measurements from all gated and non-gated images. Max-min represents the largest difference in any two measured septum thicknesses.	47
Table 2.2: Septum thickness means and ranges measured from each participant's H ⁺ MR images in two separate septum locations. Means include measurements from all gated and non-gated images. Max-min represents the largest difference in measured septum thicknesses.	47
Table 3.1: Mean Sodium Signal Intensities of Calibration Vials for Three Repeated Scans .	62
Table 3.2: Group Averages of Sodium Signal Ratios for Phantom Corrected Images.....	65

List of Figures

Figure 1.1: Labelled diagram of the human kidney, including the cortex, medulla, renal artery, renal vein, and ureter. Created with BioRender.com.	3
Figure 1.2: Labelled diagram of the nephron, including the renal corpuscle: the glomerulus and Bowman’s capsule, and the renal tubule: the proximal tubule, loop of Henle, distal convoluted tubule, and collecting duct. Created with BioRender.com.....	4
Figure 1.3: Labelled diagram of a dialyzer, indicating the direction of blood flow through the hollow fibres and the direction dialysate fluid flow. Created with BioRender.com.....	8
Figure 1.4: Labelled diagram of the heart, including its chambers, valves, arteries, veins, and septum. Created with BioRender.com.	10
Figure 1.5: Visual representation of the change in myocyte membrane potential due to movement of ions through channels in the cell membrane over the duration of a cardiac action potential. Created with BioRender.com.	12
Figure 1.6: Placement location of ECG leads on patient's chest and resulting ECG signal of voltage versus time. Representation of ECG signal includes labelled P wave, T wave, and QRS complex. Created with BioRender.com.	13
Figure 1.7: Visual representation of the LV pressure, LV volume, and electrical conductance of the heart throughout one cardiac cycle, as well as systole and diastole phases. EDV and ESV are labelled in green and red respectively. Created with BioRender.com.	14
Figure 1.8: Short-axis image of healthy heart acquired with H^+ MRI. Labelled: right ventricle, left ventricle, papillary muscles, and left ventricular wall. Pink and purple contours represent a step in LVMI measurement. Contours are drawn around the LV wall and include papillary muscles. This image is from unpublished data in the McIntyre lab.	17
Figure 1.9: Visual representation of hydrostatic (P) and osmotic (π) pressures between the capillary and interstitial space, and the direction of fluid flow caused by these pressures. Created with BioRender.com.....	19

Figure 1.10: Visual representation of a human cell with the intracellular and extracellular concentrations of essential ions, and a depiction of the Na ⁺ /K ⁺ ATPase pump. Created with BioRender.com.	20
Figure 1.11: Labelled diagram of an MRI machine, including the bore, main magnet and coils, and patient table. Created in BioRender.com.....	26
Figure 1.12: Magnetization of nuclei a) while aligned with main magnetic field, b) immediately after an RF pulse, and c) after relaxation back to direction of main magnetic field. Direction of net magnetization (M) and main magnetic field (B ₀) indicated at each step. Created with BioRender.com.....	26
Figure 1.13: Graphical representation of the a) longitudinal relaxation and b) transverse relaxation of nuclei after an RF pulse. T1 and T2 times indicated on graph. Created with BioRender.com.	27
Figure 1.14: Graphical representation of k-space with radial trajectories for image acquisition with DA2DPR pulse sequence. Spheres indicate k-space samples that are closer together towards the end of trajectories to proportionately sample k-space. Created with BioRender.com.	32
Figure 2.1: Visual representation of the regions of the cardiac cycle during which data was collected for the images containing a) 25%, b) 50%, c) 75%, and d) 100% of data from the cardiac cycle. The R-R interval here represents one full cardiac cycle.	39
Figure 2.2: Short-axis H ⁺ MR images of one participant's heart depicting the line profile location oriented a) horizontally and b) at a 45-degree angle.....	41
Figure 2.3: Short-axis Na ⁺ MR images of one participant's heart depicting the line profile location oriented a) horizontally and b) at a 45-degree angle.....	42
Figure 2.4: Plot showing the a) 18 line profiles and b) one average line profile across the septum in a horizontal direction for one participant's H ⁺ MR image before gating. The measured septum width is shown at full width half minimum with respect to the closest local maximum.	42

Figure 2.5: Plot showing the a) 18 line profiles and b) one average line profile across the septum in a horizontal direction for one participant’s Na⁺ MR image before gating. The measured septum width is shown at full width half minimum with respect to the closest local maximum. 43

Figure 2.6: Sodium images from one participant reconstructed using a) 25%, b) 50%, c) 75%, and d) 100% of data from the cardiac cycle. 43

Figure 2.7: Visual representation of an isolated pixel with its corresponding point spread function (PSF) for an ideal image and images containing 25%, 50%, and 100% of data from the cardiac cycle for one participant. The PSF represents signal intensity vs distance from the center of the pixel. One pixel is 3mm wide. 44

Figure 2.8: Point spread functions (PSFs) of pixels from images containing 25% (blue), 50% (red), and 100% (yellow) of the cardiac cycle of one participant plotted on the same graph. The PSFs represent signal intensity vs distance from the center of the pixel. The full-width-at-half-max (FWHM) for all PSFs is positioned on the graph. One pixel is 3mm wide. 45

Figure 2.9: Participant mean SNR for each tissue type separated by the percent of the cardiac cycle data sampled in the image. A square root function was fit to the data for the RV ($R^2=0.9990$), LV ($R^2=0.9995$), septum ($R^2=0.9998$), and skin ($R^2=0.9995$)..... 46

Figure 2.10: Line profiles and septum width measurements from sodium images of one participant containing data from a) 25%, b) 50%, c) 75%, and d) 100% of the cardiac cycle. 48

Figure 3.1: Flow chart displaying an overview of the project methods..... 54

Figure 3.2: Phantom experimental setup in the a) axial plane and in the b) coronal plane showing the location of the vial and c) vitamin pills within the coil. The phantom contained 150mM of NaCl and the external calibration vial contained 100mM of NaCl. 56

Figure 3.3: Visual representation of the arrangement of vials with respect to the RF coil. Values represent the concentration of NaCl in each vial in millimoles per liter. 56

Figure 3.4: a) Arrangement of coil and vials with concentrations. b) The original, c) self-corrected, and d) phantom corrected Na⁺ MR calibration images of one of the three calibration scans..... 61

Figure 3.5: Mean vial sodium signal intensities versus known sodium concentration. Each data point represents the mean of three vial signal intensity measurements. Error bars represent the standard deviation values for each data point. 62

Figure 3.6: Mid-short-axis slice acquired by a) proton and b) sodium MRI. Proton and sodium images are superimposed in image c). Increased intensity in the sodium image represents higher sodium concentration in that region. 63

Figure 3.7: The a) original cardiac Na⁺ MR image of one participant, and the image after b) self-correction, and c) phantom correction with regions of interest (ROIs) displayed. The ROIs are labelled to show the right ventricle (RV), left ventricle (LV), and septum (S). Coil location shown. 63

Figure 3.8: Mean sodium signal ratios for the original cardiac sodium images. Ratios are separated by participant number and ratio type. Ratios include the mean signal in the septum over the mean signal in the right ventricle (RV), left ventricle (LV), average signal in both ventricles (AVG), and external 100mM NaCl vial. Error bars represent the uncertainty in each ratio, calculated from the standard deviations of the signal intensities in each ROI..... 64

Figure 3.9: Mean sodium signal ratios for the phantom corrected cardiac sodium images. Ratios are separated by participant number and ratio type. Ratios include the mean signal in the septum over the mean signal in the right ventricle (RV), left ventricle (LV), average signal in both ventricles (AVG), and external 100mM NaCl vial. Error bars represent the uncertainty in each ratio, calculated from the standard deviations of the signal intensities in each ROI. 65

List of Abbreviations

α - Flip Angle

γ - Gyromagnetic Ratio

ω_0 – Larmor Frequency

H^+ – Proton

Na^+ – Sodium

ANP – Atrial Natriuretic Peptide

ATP – Adenosine Triphosphate

ATPase – Adenosine Triphosphatase

AV – Atrioventricular

B_0 – Main Magnetic Field

ECG – Electrocardiogram

Ca^{2+} - Calcium

CKD – Chronic Kidney Disease

CO – Cardiac Output

CVD – Cardiovascular Disease

DA2DPR – Density Adapted 2-dimensional Projection Reconstruction

DA3DPR – Density Adapted 3-dimensional Projection Reconstruction

EDV – End Diastolic Volume

eGFR – Estimated Glomerular Filtration Rate

ESV – End Systolic Volume

FIESTA – Fast Imaging Employing Steady-state Acquisition

FOV – Field of View

FWHM – Full Width at Half Maximum

GFR – Glomerular Filtration Rate

H^+ - Proton

HD – Hemodialysis

K^+ - Potassium

LV – Left Ventricle

LVEF – Left Ventricular Ejection Fraction

LVH – Left Ventricular Hypertrophy

M – Magnetization
MIF – Myocardial Interstitial Fibrosis
MR – Magnetic Resonance
MRI – Magnetic Resonance Imaging
Na⁺ - Sodium
NaCl – Sodium Chloride
OA – Osmotically Active
OI – Osmotically Inactive
PSF – Point Spread Function
RAAS – Renin Angiotensin Aldosterone System
RF – Radiofrequency
ROIs – Regions of Interest
RV – Right Ventricle
SA – Sinoatrial
SGLT-2 – Sodium Glucose Co-transporter 2
SNR – Signal-to-Noise Ratio
SV – Stroke Volume
T - Tesla
T1 – Spin-lattice Relaxation
T2 – Spin-spin Relaxation
TE – Echo Time
TR – Repetition Time

Chapter 1

1 Introduction

This thesis assesses the utility of technical adaptations for cardiac sodium (Na^+) magnetic resonance imaging (MRI). These technical adaptations include electrocardiogram (ECG) gating and the correction of image signal intensity non-uniformity. This introductory chapter provides background information related to biological Na^+ , chronic kidney disease, hemodialysis, cardiovascular disease risk, proton (H^+) MRI and Na^+ MRI. The following sections of this chapter will provide the introduction and motivation for this thesis research project.

1.1 Motivation and Overview

CKD is defined as structural or functional damage to the kidneys that has persisted for longer than 3 months. This damage reduces their ability to filter the blood, which otherwise maintains water, ion, and pH balance and removes toxins. CKD is a prominent health issue worldwide, with the global prevalence recently recorded to be 9.1%.¹ It is also well established that patients with CKD are at an increased risk for developing cardiovascular disease (CVD). Although it is apparent that CKD and CVD are closely related, the direct link between these diseases remains unclear. Many studies have confirmed the presence of diffuse myocardial interstitial fibrosis using spin-lattice relaxation (T1) mapping of heart tissue and demonstrated left ventricular hypertrophy (LVH) in the hearts of CKD patients.²⁻⁶ Studies have also shown CKD patients to have Na^+ accumulation in different regions of their bodies, as their kidneys have impaired excretion of sodium.⁷ Since Na^+ is a ion involved in many important biological processes, especially in the myocardium, it is possible that a Na^+ imbalance may be related to cardiac abnormalities in CKD patients. Na^+ MRI is a valuable non-invasive imaging modality that can evaluate the Na^+ content of tissues including the myocardium.⁸ It would be beneficial to use Na^+ MRI for investigating the correlations between myocardial fibrosis, left ventricular (LV) dysfunction, and myocardial Na^+ content in CKD patients. Investigating the potential build-up of Na^+ in the myocardium is important, as other

studies have found instances of Na^+ accumulation to influence many signal pathways and correlate with several adverse biological processes, such as ischemia, inflammation, and fibrosis.⁹⁻¹¹ However, before it's possible to use cardiac Na^+ MRI to extract and compare image data between individuals, many technical adaptations must be addressed.

Specifically, should ECG gating be implemented to remove cardiac motion during imaging? And is the signal intensity nonuniformity created by surface coil imaging able to be corrected for?

In this thesis, the hearts of healthy participants are imaged using cardiac Na^+ MRI to determine the technical adaptations needed for imaging before applying the modality to a future patient study. Chapter 1 provides an outline of the background information, techniques used, and motivation for this thesis. Chapter 2 evaluates the effects of ECG gating on Na^+ MR image quality using a 3-Tesla (T) clinical scanner. Chapter 3 evaluates the effectiveness of an intensity correction method that uses Na^+ phantom images by first testing it on Na^+ calibration images before applying it to the cardiac images themselves.

1.2 The Kidney

This section provides an overview of the anatomy and physiology of the kidneys while extending these concepts to states of disease.

1.2.1 Kidney Anatomy

The kidneys are two bean-shaped organs located in the middle-back portion of the abdominal cavity and lay on either side of the spine. They are located between the membranes that line the abdomen and the bones and muscles of the back. This positioning is named retroperitoneal. The kidneys are connected to the blood stream through the renal artery and vein, and they are connected to the bladder through the ureter. These structures are attached to the kidneys at the inner concave side. The kidneys themselves consist of an outer layer named the cortex and an inner layer named the medulla. Figure 1.1 presents a labelled diagram of the kidney anatomy.

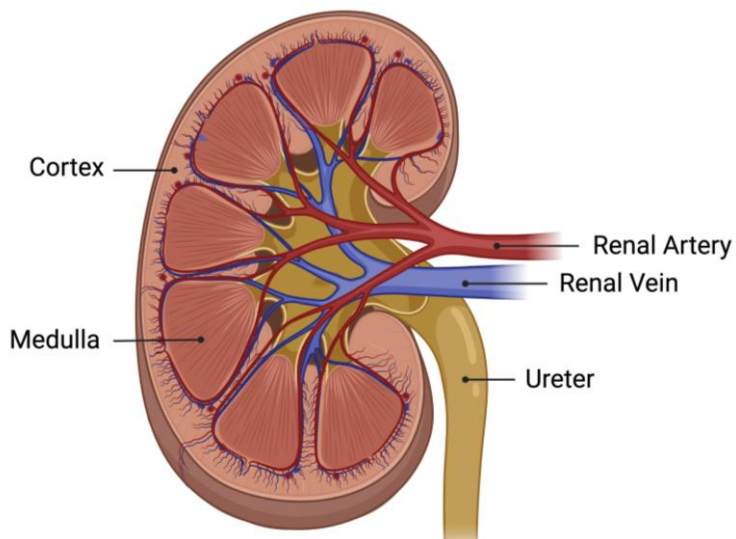


Figure 1.1: Labelled diagram of the human kidney, including the cortex, medulla, renal artery, renal vein, and ureter. Created with BioRender.com.

The functional units of the kidneys are located in the cortex and are referred to as nephrons. The nephron consists of two main parts: the renal corpuscle and the renal tubule (Figure 1.2). Within the renal corpuscle is a capillary bed known as the glomerulus which is surrounded by a structure called Bowman's capsule. The renal tubule is a long tubular structure that can be broken down into four main sections: the proximal tubules, loop of Henle, distal convoluted tubule, and collecting duct. There are approximately 1.2 million nephrons in each kidney that are surrounded by networks of blood vessels.¹²

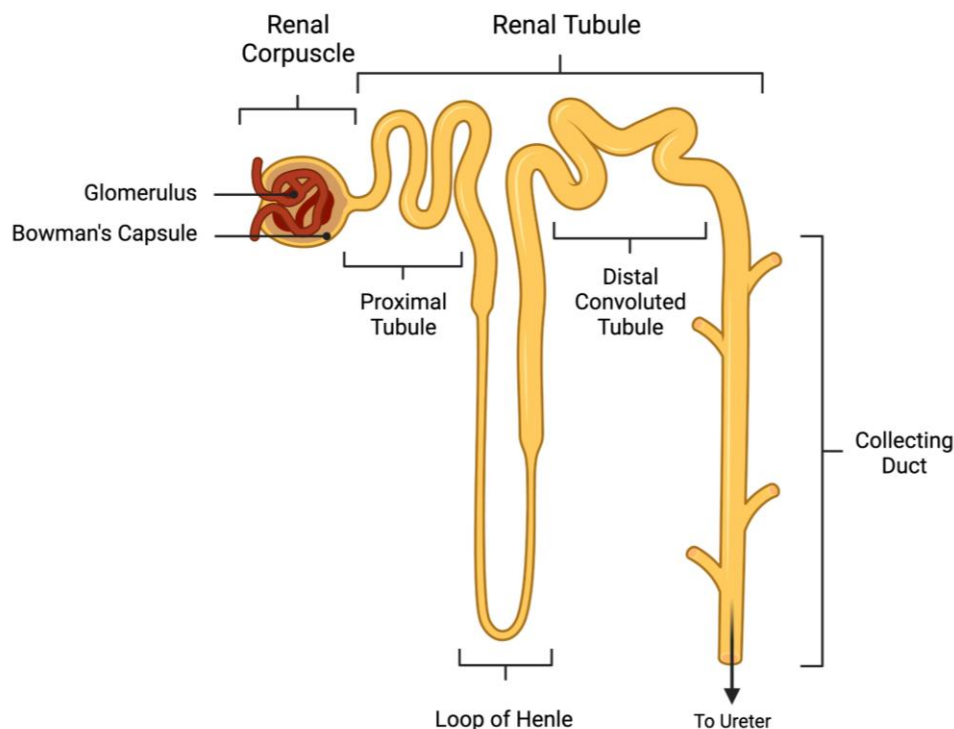


Figure 1.2: Labelled diagram of the nephron, including the renal corpuscle: the glomerulus and Bowman's capsule, and the renal tubule: the proximal tubule, loop of Henle, distal convoluted tubule, and collecting duct. Created with BioRender.com.

1.2.2 Kidney Physiology

The kidneys have many essential functions including controlling acid-base and water balances, maintaining electrolyte balance, removing waste and toxins, controlling blood pressure, and producing hormones. These processes occur as blood enters the kidneys through the renal artery and is filtered by the nephrons. The waste that remains in the nephrons at the end of filtration is sent through the ureter to be stored in the bladder as urine, and the filtered blood exits the kidneys through the renal vein.

Blood initially enters the nephron through the afferent arteriole and into the glomerulus where filtration occurs. Almost all components of the blood besides red and white blood cells and proteins are filtered into Bowman's capsule to produce a fluid called the ultrafiltrate. The components of the blood that remain in the glomerulus exit through the

efferent arteriole and remain in the blood vessels surrounding the nephron. The filtrate in Bowman's capsule proceeds through the renal tubule where water, ions, glucose, and amino acids are reabsorbed from the filtrate to surrounding capillaries. Secretion of molecules from surrounding capillaries into the filtrate in the tubule can also occur. At the end of the collecting duct is a concentrated filtrate of wastes also known as urine. The amount of solute excreted by the body in urine depends on the amount filtered into Bowman's capsule, the amount reabsorbed into surrounding capillaries, and the amount secreted into the tubule by these capillaries.

Kidney function can be measured by the amount of fluid/solutes that are filtered per unit time from the glomerulus into Bowman's capsule. This is known as the glomerular filtration rate (GFR). GFR cannot easily be directly measured in an individual and therefore an estimated glomerular filtration rate (eGFR) is used to measure kidney function instead. A substance called creatinine is used to measure eGFR because it is a waste substance that is almost fully excreted and therefore gives a convenient indication of glomerular filtration. To measure eGFR the creatinine concentration in blood is needed. A normal eGFR is usually around 125 mL/min, but can differ depending on age, sex, and body size.¹²

1.2.3 Sodium (Na^+) Handling by the Kidney

Sodium can be excreted from the body through sweat, feces, and urine. Of particular interest to this thesis, the kidney is the main excretory mechanism for biological Na^+ .¹³ Although in most healthy individuals, less than one percent of the amount of Na^+ that was initially filtered into Bowman's capsule is excreted from the body in the urine. The kidney is able to alter the excretion of Na^+ in order to maintain Na^+ homeostasis.

Along the length of the renal tubule, there are many transporters and channels that assist in the reabsorption of Na^+ into the surrounding capillaries, and some of them are regulated by hormones. Some channels that reabsorb Na^+ in the proximal tubule are regulated by a hormone called angiotensin II and some in the collecting duct are regulated by aldosterone. Angiotensin II and aldosterone are hormones that are a part of the renin-angiotensin aldosterone system (RAAS). The RAAS is a multi-step system that

regulates Na^+ balance and therefore blood pressure. A hormone called renin is released by the kidneys when low blood pressure or low levels of Na^+ in the blood are detected. Renin catalyzes one of the steps in the processes of angiotensin II formation. Angiotensin II acts on channels in the proximal tubule to increase Na^+ reabsorption. It also acts on the adrenal glands to stimulate production of aldosterone, which act on channels in the collecting duct to increase Na^+ reabsorption. The result is increased Na^+ retention and therefore increased blood pressure.

Atrial natriuretic peptide (ANP) is another hormone that regulates Na^+ excretion by the kidneys. When there are high concentrations of Na^+ in the blood, high extracellular volume, and high blood pressure, the walls of the cardiac atria distend and release ANP into the bloodstream. ANP goes to inhibit aldosterone release from the adrenal glands and dilates the afferent arteriole to increase GFR. This process decreases the reabsorption of Na^+ in the collecting duct and increases the amount of Na^+ filtered into Bowman's capsule. The result is increased Na^+ excretion by the kidneys.

Another important process by which the kidneys regulate Na^+ balance is tubuloglomerular feedback. Through this process, the GFR is regulated based on the contents of the ultrafiltrate. Specialized cells detect the amount of Na^+ in the renal tubule and constrict the afferent arteriole if the Na^+ levels are too high. This reduces the GFR and therefore reduces the amount of Na^+ filtered into Bowman's capsule.

1.2.4 Chronic Kidney Disease (CKD)

In a 2017 study, there was a 9.1% global prevalence of all-stage CKD.¹ CKD is defined as kidney structural or functional damage for more than three months. Certain conditions cause kidney function to decline, with hypertension and diabetes being the two most common causes of CKD. There are five stages of CKD based on the patient's eGFR which is expressed in relation to body surface area. Table 1.1 gives an overview of the five stages of CKD.¹⁴ Overall, CKD is a collective term for any damage to the kidneys that results in decreased GFR, and is therefore not specific. CKD often occurs alongside various other health complications and is a major risk factor of morbidity and mortality.

Table 1.1: The Five Stages of CKD with eGFR Values

	eGFR (mL/min/1.73m²)	Kidney Function
Stage 1	≥ 90	Normal or high
Stage 2	60-89	Mildly decreased
Stage 3	30-59	Moderately decreased
Stage 4	15-29	Severely decreased
Stage 5	< 15 (or on hemodialysis)	Kidney failure

1.2.4.1 Hemodialysis (HD)

Patients with CKD that have an eGFR of < 15 mL/min/1.73m² or lose more than 85-90% of their kidney function are normally placed on dialysis therapy. The most common type of dialysis therapy is hemodialysis (HD). The purpose of this treatment is to mimic a fully functioning kidney by filtering the blood and restoring the intracellular and extracellular fluid environment. During HD, the patient's blood is pumped outside of the body and through an artificial kidney machine or dialyzer before returning back to the patient. The dialyzer is a tube that contains a bundle of very thin hollow fibres, where the fibre material itself is a semi-permeable membrane. Blood flows through the center of the hollow fibres in one direction, and the dialysate fluid surrounds the fibres and flows in the opposite direction (Figure 1.3). The dialysate is a solution of water, electrolytes, and salts. Its composition dictates the filtration of the blood and can be modified depending on clinical need. As the blood flows through the dialyzer, waste and excess fluids pass through the semi-permeable membrane and are removed by the dialysate fluid. This occurs through the diffusion of molecules from an area of higher to lower concentration, and ultrafiltration of fluids from areas of higher to lower pressure.¹⁵

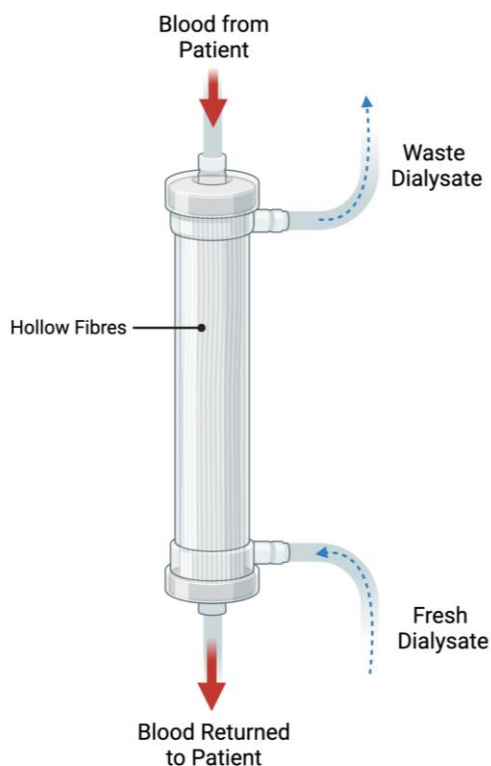


Figure 1.3: Labelled diagram of a dialyzer, indicating the direction of blood flow through the hollow fibres and the direction dialysate fluid flow. Created with BioRender.com.

Patients on HD have an additional mechanism of Na^+ excretion, which is through dialysis due to their minimal kidney function. During dialysis, most of the Na^+ is removed by ultrafiltration rather than diffusion.¹⁶ Therefore, the amount of Na^+ removed depends mostly on the amount of fluid removed, with diffusion fine tuning the Na^+ removal.

Most commonly, patients on HD receive treatment three times a week for about four hours per session. Although there have been many technical and scientific improvements in the HD treatment, hemodialysis cannot perfectly replicate healthy kidney function. Patients on HD are at increased risks for developing additional conditions, such as electrolyte abnormalities, anemia, infection, and cardiovascular dysfunction, therefore the risks of morbidity and mortality are significantly elevated for these individuals.¹⁷⁻¹⁹

1.3 The Heart

This section provides an overview of the anatomy and physiology of the heart while extending these concepts to states of disease.

1.3.1 Cardiac Anatomy

The human heart is a muscular organ about the size of a fist, and is located in the center of the chest, slightly to the left. The heart is the central pump of the cardiovascular system consisting of walls, chambers, valves, arteries, veins, and an electrical conduction system. The anatomy of the heart can be visualized in Figure 1.4. The heart consists of four chambers: the right atrium, left atrium, right ventricle, and left ventricle. The septum is the portion of these chamber walls that divides the heart into its left and right sides. There are 4 important valves that separate each of the chambers: the right atrioventricular (AV) or tricuspid valve, the pulmonary semilunar valve, the left AV or bicuspid valve, and the aortic valve. The major veins connecting to the heart include the superior and inferior vena cava and the pulmonary veins, whereas the major arteries connecting to the heart include the pulmonary arteries and the aorta. The heart also contains an electrical conduction system with specialized nodal and conducting cells. These cells make up the sinoatrial (SA) node, AV node, bundle of His, and Purkinje fibers.

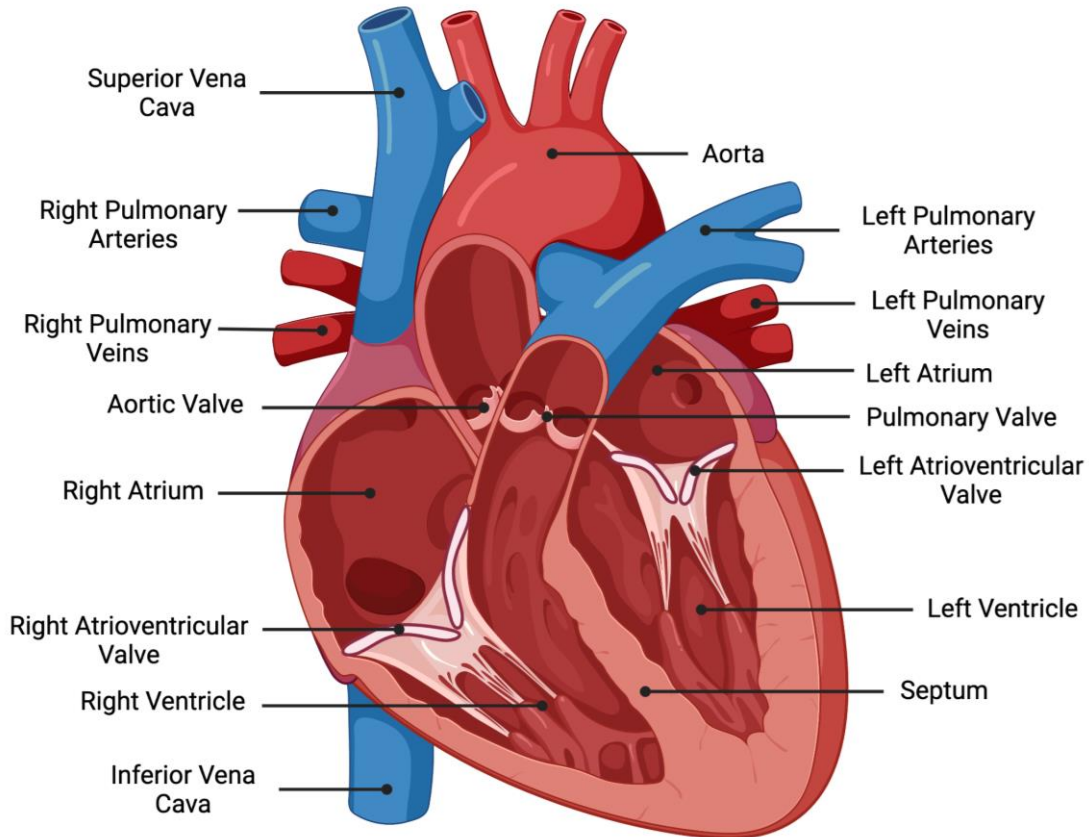


Figure 1.4: Labelled diagram of the heart, including its chambers, valves, arteries, veins, and septum. Created with BioRender.com.

1.3.2 Cardiac Physiology

The main function of the heart is to pump blood throughout the body to deliver oxygen, nutrients, and hormones to all tissues while regulating body temperature. The heart serves these functions by pumping oxygen-poor blood into the pulmonary circulation to reach the lungs and pumping oxygen-rich blood into the systemic circulation to reach the remainder of the body. It is the atria that receive blood from major veins, and the ventricles that pump blood throughout the circulation with the help of major arteries. The left ventricle is the main pumping chamber of the heart, and the walls of this chamber are very thick and muscular because they must contract with a great amount of force to pump blood into the systemic circulation. This is one of the reasons why the left ventricular wall, and specifically the septum, are of particular interest in this thesis.

The blood flows through the heart in one direction. This begins with the right side of the heart as oxygen-poor blood is received by the superior and inferior vena cava, flows through the right atrium and ventricle, and is pumped to the lungs through the pulmonary arteries. Once this blood is re-oxygenated, it returns to the left side of the heart through the pulmonary veins, flows through the left atrium and ventricle, and is pumped to the rest of the body through the aorta. It is each of the four valves that prevent the backflow of blood throughout this process.

The electrical conduction system controls the heart's rhythmic contractions. This system is responsible for generating an electrical stimulus and allowing it to travel throughout the heart. The electrical stimulus begins in the SA node, transfers to the atrioventricular AV node, extends through the bundle of His, and finally travels through the Purkinje fibers to contract both atria then both ventricles in synchrony. These cells are organized in such a way that the atria contract from top down to push blood down into the ventricles, and the ventricles contract from bottom up to push blood out into the circulation.

At the cellular level, the heart is made up of muscle cells called cardiac myocytes. These myocytes produce action potentials with the movement of ions through channels in the cell membrane to change the membrane electrical potential and allow muscle contraction. The ions involved in this process include Na^+ , calcium (Ca^{2+}), and potassium (K^+).²⁰ Figure 1.5 shows a representation of the cardiac action potential. The cardiac muscle cells are tightly bound to one another to allow this electrical impulse to travel quickly throughout the heart.

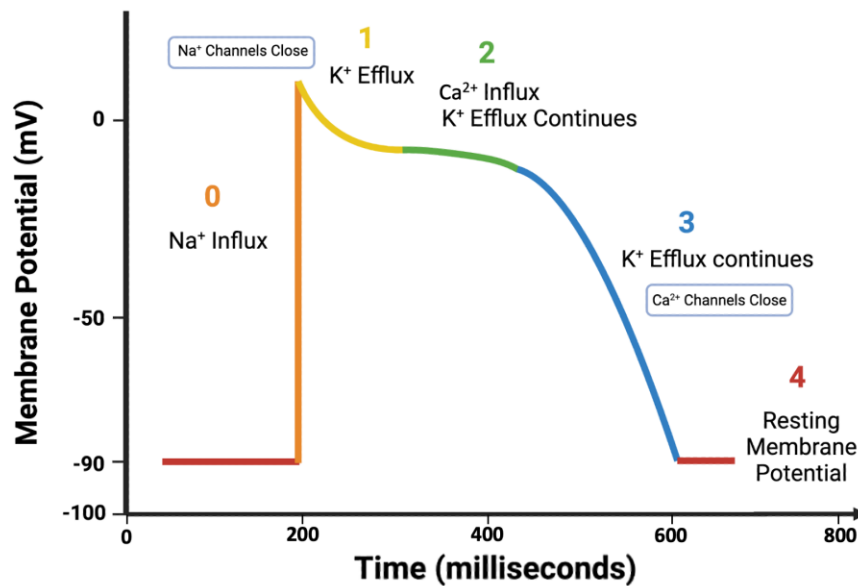


Figure 1.5: Visual representation of the change in myocyte membrane potential due to movement of ions through channels in the cell membrane over the duration of a cardiac action potential. Created with BioRender.com.

The electrical conductance of the heart can be measured by an ECG, which is recorded by placing leads on the patient's chest to detect the electrical potential of the heart throughout the cardiac cycle. The ECG is a graph of voltage versus time of the heart's electrical activity which can be broken down into the P wave, QRS complex, and T wave (Figure 1.6). The P wave represents the depolarization of atrial muscle, and QRS complex is the depolarization of ventricular muscle, and the T wave is the repolarization of ventricular muscle. The ECG trace of an individual can provide information on their heart rate and can evaluate disturbances in rhythm or conduction.

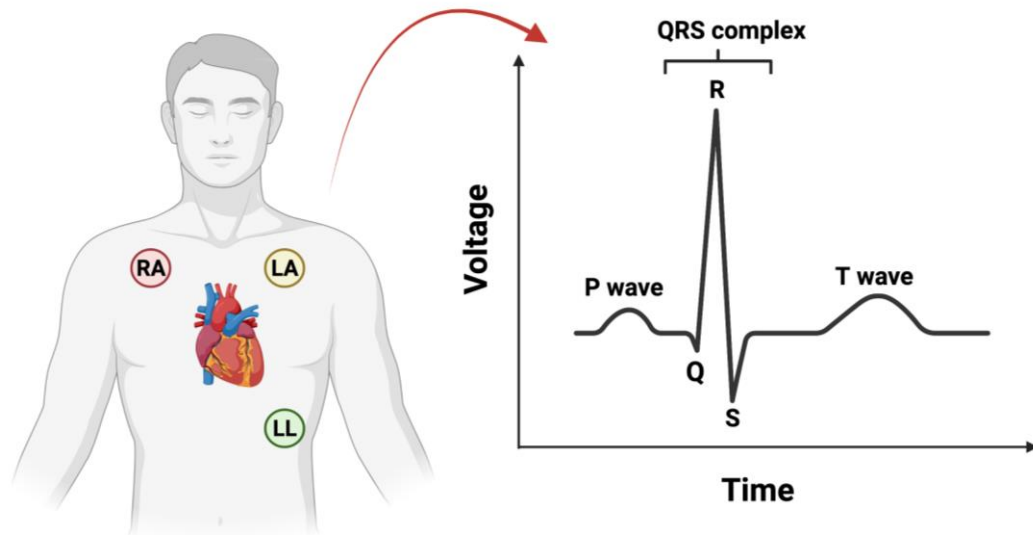


Figure 1.6: Placement location of ECG leads on patient's chest and resulting ECG signal of voltage versus time. Representation of ECG signal includes labelled P wave, T wave, and QRS complex. Created with BioRender.com.

Overall, the cardiac cycle is separated into two main phases: systole and diastole. Systole occurs when the heart contracts to eject the blood, and diastole occurs when the heart muscle relaxes to fill with blood. Figure 1.7 gives a representation of the pressure, volume, and electrical conductance of the heart throughout the cardiac cycle.

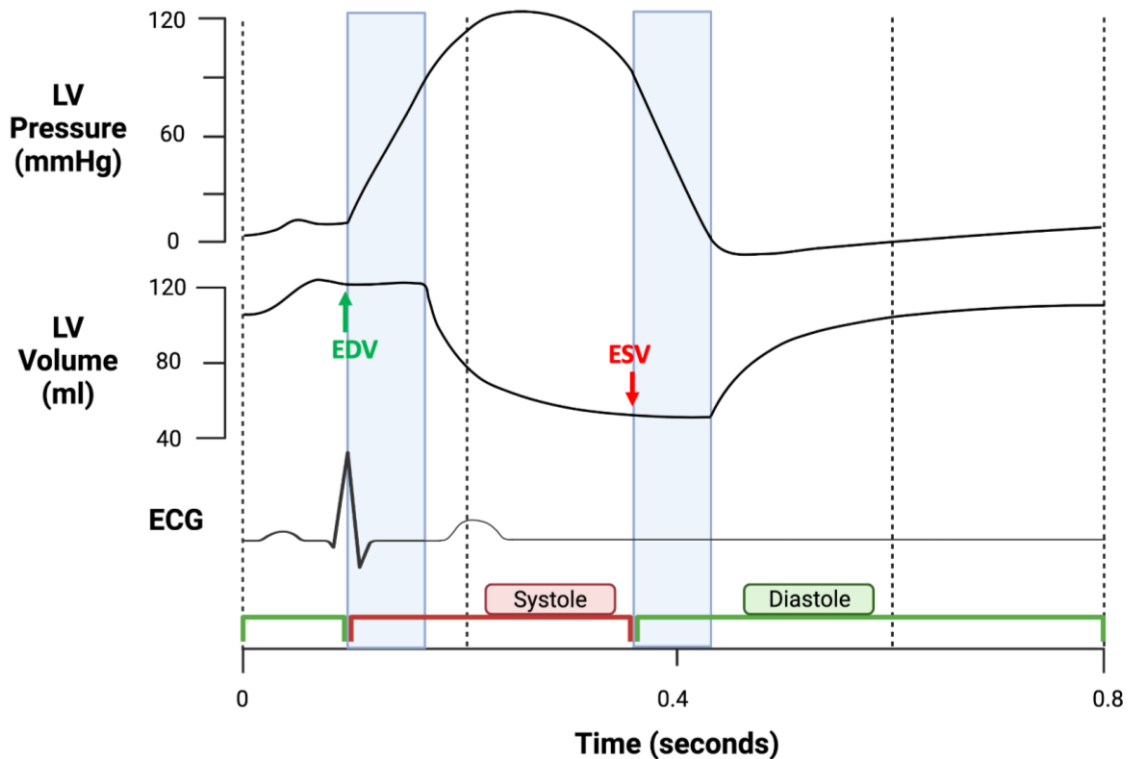


Figure 1.7: Visual representation of the LV pressure, LV volume, and electrical conductance of the heart throughout one cardiac cycle, as well as systole and diastole phases. EDV and ESV are labelled in green and red respectively. Created with BioRender.com.

There are a few parameters that are important for assessing the mechanical performance of the heart. These parameters include end diastolic volume (EDV), end systolic volume (ESV), stroke volume (SV), cardiac output (CO), and left ventricular ejection fraction (LVEF). EDV is the amount of blood in milliliters in the ventricles at the end of ventricular diastole (just before contraction), and ESV is the amount of blood in the ventricles at the end of systole (just after contraction). Using these parameters we can calculate SV, the amount of blood pumped by the ventricles during one contraction.

$$\text{Stroke Volume (SV)} = \text{EDV} - \text{ESV} \quad [1.1]$$

CO explains the amount of blood that is pumped by the ventricles in one minute in units of liters per minute. CO is calculated using the following equation:

$$\text{Cardiac Output (CO)} = \text{Heart rate (HR)} \times \text{Stroke Volume (SV)} \quad [1.2]$$

LVEF is another important cardiac parameter that explains the amount of blood that's pumped out of the LV in one heartbeat, and it's typically expressed as a percent of blood that was in the ventricle prior to contraction. LVEF is calculated using the following equation:

$$\text{Left Ventricular Ejection Fraction (LVEF)} = \frac{SV}{EDV} \times 100 \quad [1.3]$$

1.3.3 Cardiovascular Disease (CVD) in CKD Patients

Cardiovascular disease (CVD) is a term used to address a group of disorders of the heart and blood vessels. It has been determined that patients with CKD are at an elevated risk for developing CVD from an early stage, but the exact mechanism interrelating these diseases remains unclear. CVD is the leading cause of death worldwide and in the CKD population.²¹ Patients with CKD are more likely to experience cardiovascular complications or death than progression to end-stage renal disease.¹⁷ CVD in CKD patients differs from CVD in the general population because the outcomes in CKD patients are not fully accounted for by the traditional risk factors for these diseases, such as age, family history, obesity, diabetes mellitus, and increased blood pressure and volume. In CKD patients, cardiovascular complications include the traditional and non-traditional risk factors. The adverse cardiovascular complications associated with patients with CKD are often collectively termed uremic cardiomyopathy, and include complications such as coronary artery disease, arterial stiffness, calcification, inflammation, and myocardial stunning that can lead to sudden cardiac death.²²

In patients with CKD, the heart as well as its vascular system undergo structural and functional remodeling. Coronary artery disease is extremely prevalent in CKD patients and involves the build-up of plaque in the arteries that supply the heart with oxygen-rich blood.²³ These same arteries are also known to become stiff and develop calcifications, specifically in patients with CKD stage 5 and are predictors of all-cause and cardiovascular mortality.²⁴ Vascular calcification and stiffness have been found to correlate with one another, although the mechanisms by which these issues relate remains

unknown.²⁵ CKD is also known to cause a chronic inflammatory state in the body that is the result of a multitude of factors such as acidosis, oxidative stress, increased pro-inflammatory cytokines, and increased numbers of infections. This inflammatory state contributes to the cardiovascular complications these patients experience, and it is especially prevalent in those on hemodialysis.²⁶ The hemodialysis therapy itself can cause myocardial stunning: reductions in LV wall motion due to repetitive interruptions in blood flow.²⁷ Continuous renal replacement therapy can lead to permanent LV dysfunction as the damage from these ischemic events are cumulative and persist even after reperfusion.^{28,29} Each of these factors come together to increase the risks of heart failure, arrhythmia, and sudden cardiac death in individuals with CKD.

Even with this knowledge, the manifestation of CVD in CKD remains unclear with many different factors at play. Much additional research must be conducted to address this comorbidity. In recent work, two cardiovascular complications that have been found to be of specific interest in patients with CKD include diffuse myocardial interstitial fibrosis and LVH.^{22,30}

1.3.3.1 Myocardial Interstitial Fibrosis (MIF)

Fibrosis is a scarring event that can present itself in different manners depending on the disease. It is common for patients that have experienced a myocardial infarction to have fibrosis localized to the cardiac tissue affected,³¹ but patients with CKD most commonly experience a diffuse pattern of fibrosis termed myocardial interstitial fibrosis (MIF).⁵ MIF is the diffuse excess deposition of fibrous tissue or collagen in the extracellular matrix of the myocardium. Collagen is the main structural protein in the human body and can contribute to stiffness and therefore LV dysfunction when it accumulates in the myocardium.^{32,33} Biopsy and imaging studies have confirmed that patients with CKD have high levels of MIF that correlate with stage of CKD and length of time on dialysis.^{34,35} It has also been found that there is no progression in MIF biomarkers if kidney function remains stable in patients with early-stage CKD.³⁶ There is an unmet medical need of connecting the incidence of MIF with CKD. It is predicted that the progressive loss of kidney function initiates mechanisms that stimulate the production of MIF in CKD patients. MIF itself leads to LV dysfunction, arrhythmias, disruptions in

myocardial perfusion, and can therefore be used to help predict cardiovascular outcomes in CKD patients.⁵

1.3.3.2 Left Ventricular Hypertrophy (LVH)

Left ventricular hypertrophy (LVH) is characterized by the enlargement of the heart's left ventricle caused by increased cardiomyocyte size. LVH is usually diagnosed based on the calculated LV mass, but normal values will change based on the age, sex, and body surface area of the individual.^{37,38} For this reason, values of LV mass are commonly reported as LV mass index (LVMI) which is the mass of the LV indexed to the body surface area in units of g/m^2 . In general, normal values of LVMI (mean \pm standard deviation) for women are $49 \pm 10 \text{ g}/\text{m}^2$ and $62 \pm 11 \text{ g}/\text{m}^2$ for men.³⁹ These values are based on the inclusion of the papillary muscles in the LVMI measurement (Figure 1.8). For the diagnosis of LVH, LVMI must be roughly $\geq 131 \text{ g}/\text{m}^2$ for men and $\geq 100 \text{ g}/\text{m}^2$ for women.³⁷

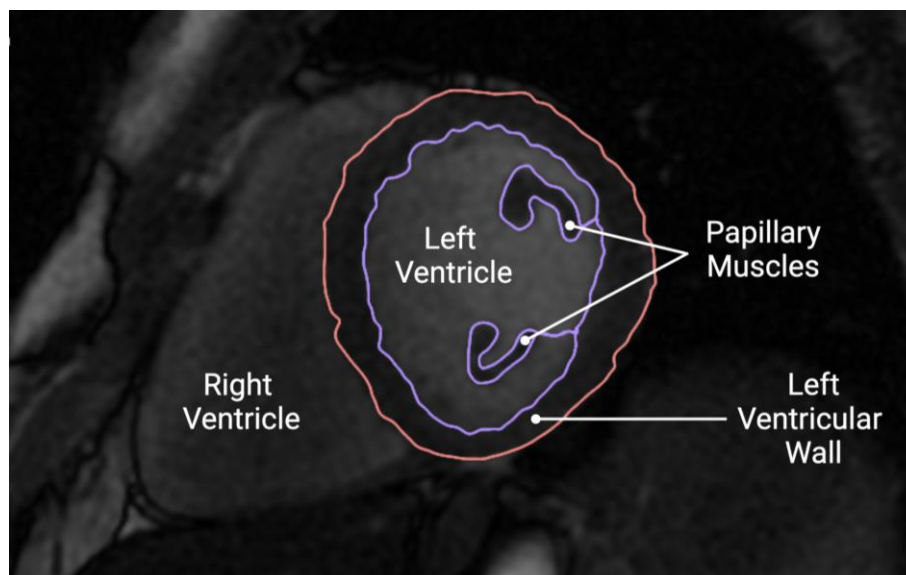


Figure 1.8: Short-axis image of healthy heart acquired with H^+ MRI. Labelled: right ventricle, left ventricle, papillary muscles, and left ventricular wall. Pink and purple contours represent a step in LVMI measurement. Contours are drawn around the LV wall and include papillary muscles. This image is from unpublished data in the McIntyre lab.

LVH is the first step of ventricular remodeling. In some cases, it occurs due to intense athletic training, but it's often the result of pathological conditions. One of the main physiological mechanisms by which LVH occurs is pressure and volume overload in the left ventricle. Cardiomyocytes counteract the increased stress to the walls of the heart by expanding and the chamber thickens to result in LVH. Aside from this mechanism, different diseases of the heart, genetics, or abnormal tissue growth in the heart muscle can also cause LVH.³⁸

It is common for patients with CKD to have LVH, with the prevalence of LVH being inversely related to patient eGFR. Patients with CKD stage 1-3 are found to have a LVH prevalence of 16-31%; 60-75% for stage 4-5; and over 90% once on dialysis. LVH in CKD patients has been found to be associated with cardiovascular events and mortality risk, however, the pathogenesis of LVH in CKD is poorly understood.² One more recent finding is that skin Na⁺ content has been found to correlate with LVH in patients with CKD, suggesting that tissue Na⁺ levels may be a strong predictor of poor cardiovascular outcomes.⁴⁰

1.4 Biological Sodium (Na⁺)

The following sections provide a brief overview of Na⁺ in relation to the fluid compartments of the body, the importance of Na⁺, and Na⁺ in disease.

1.4.1 Fluid Compartments

The majority of the Na⁺ in the human body is found in aqueous solution.⁴¹ This aqueous solution is divided into intracellular and extracellular fluid, that contains about 2/3 and 1/3 of the total body water respectively. Na⁺ is the most prevalent cation in the extracellular fluid. This compartment can be broken down further into the fluid found in the blood (plasma) and the fluid outside of the blood (interstitial fluid). It is the Starling equation that dictates the water flux between these two compartments:

$$P_c - P_{IF} = \pi_c - \pi_{IF} \quad [1.4]$$

In this equation, P_c is the capillary hydrostatic pressure of plasma, P_{IF} is the interstitial fluid hydrostatic pressure, π_c is the capillary plasma osmotic pressure, and π_{IF} is the interstitial osmotic pressure. Hydrostatic pressure represents the pressure exerted by a fluid, and osmotic pressure represents the pressure of fluid flowing inward caused by a high concentration of solutes. The direction of the flow of fluid caused by these pressures is shown in Figure 1.9 below.

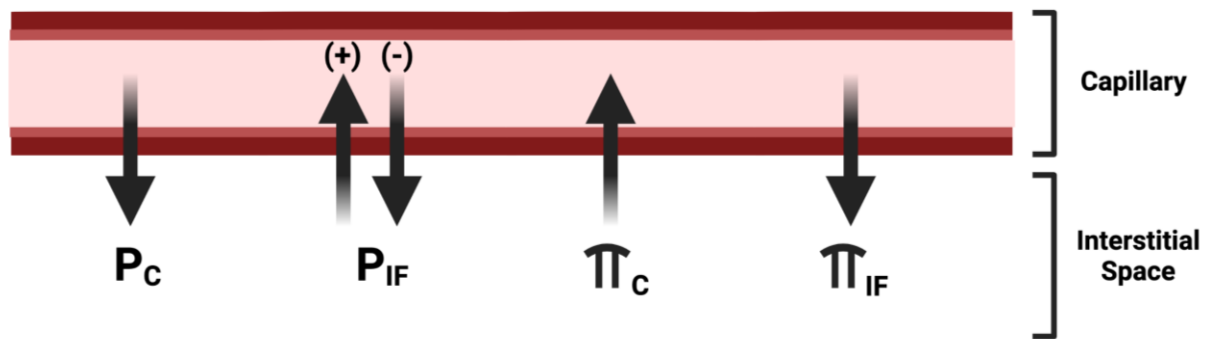


Figure 1.9: Visual representation of hydrostatic (P) and osmotic (π) pressures between the capillary and interstitial space, and the direction of fluid flow caused by these pressures. Created with BioRender.com.

1.4.2 The Role of Sodium (Na^+) in the Body

Na^+ is an essential electrolyte involved in many cellular processes including the transmission of nerve pulses, regulating the contraction and relaxation of muscles, and maintaining fluid and pH balance. Na^+ is found at a concentration of 140-150 mM in the extracellular space, and 10-15 mM in the intracellular space.^{42,43} This concentration gradient is maintained by the sodium-potassium adenosine triphosphatase (Na^+/K^+ ATPase) pump, which uses energy to pump Na^+ out of and K^+ into the cell (Figure 1.10). There are also other mechanisms of Na^+ transport through the cell membrane, such as the sodium channels that allow sodium to flow into the cell and sodium proton (Na^+/H^+) exchangers which exchange one proton for one sodium ion. Alterations in Na^+ concentrations can indicate pathological conditions and have been investigated during the study of myocardial infarction, osteoarthritis, diabetes, kidney disease, and more.^{44,45}

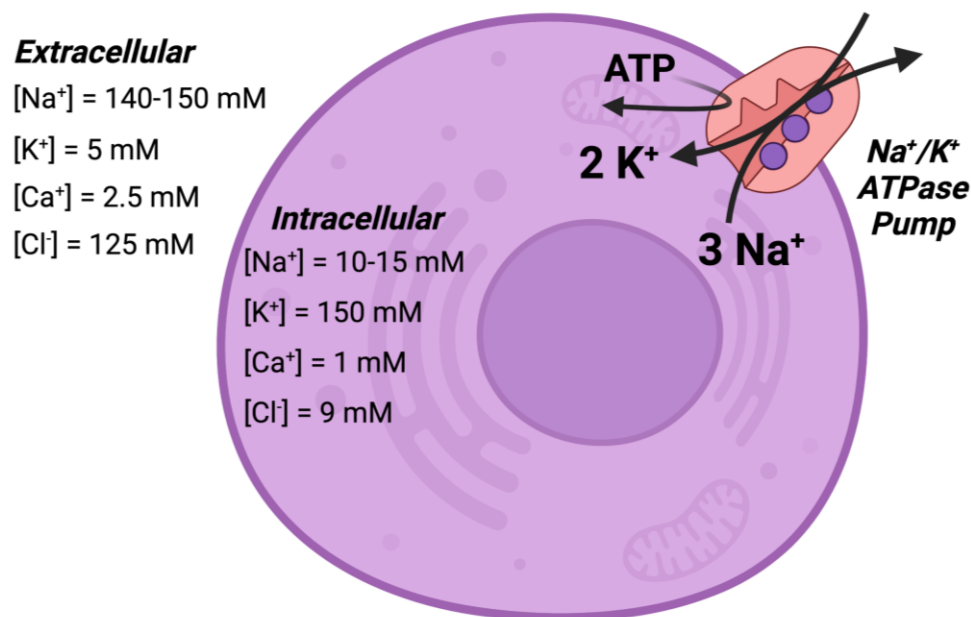


Figure 1.10: Visual representation of a human cell with the intracellular and extracellular concentrations of essential ions, and a depiction of the Na⁺/K⁺ ATPase pump. Created with BioRender.com.

1.4.3 Osmotically Inactive Sodium (Na⁺)

Na⁺ metabolism in the body has previously been considered *steady state*, where total body water and Na⁺ remain constant as excess dietary Na⁺ is eliminated by the kidneys. In this model, an increase in Na⁺ in any region of the body would be followed by an increase in water volume to maintain the Na⁺ concentration in that area. Na⁺ that acts in this manner is termed osmotically active Na⁺ (OA- Na⁺). Over the last 20 years, our understanding of Na⁺ metabolism has changed. It was discovered that Na⁺ can accumulate in tissue without being accompanied by excess water deposition.⁴⁶ This Na⁺ is termed osmotically inactive Na⁺ (OI- Na⁺), and has been found in the skeleton, soft tissues, and skin.⁴⁷⁻⁴⁹

Two mechanisms have been proposed for the accumulation of OI- Na⁺ in tissue. This first mechanism suggests that in cellular dense tissues such as muscle, excess Na⁺ may be stored intracellularly. The Na⁺ would be replacing intracellular potassium in order to maintain cellular tonicity.⁴¹ The second mechanism can be attributable to OI- Na⁺

accumulation in other tissues. In this mechanism, the positively charged Na^+ is recruited by negatively charged proteoglycans in the extracellular matrix removing its osmotic abilities. This mechanism is supported by studies showing correlations between increased proteoglycans and increased Na^+ content in the skin.⁵⁰

The accumulation of OI- Na^+ has been studied in many disease conditions and has been found to influence many biological processes and signal pathways, such as the immune response, ischemia, and hypertension. Local OI- Na^+ deposition has been linked to the immune system as it has been found to influence immune cell function and inflammation.⁹ A local increase of OI- Na^+ has also been found in regions subject to ischemia-reperfusion injury, specifically in the human myocardium.^{10,44} Additionally, hypertension has been associated with the accumulation of OI- Na^+ in the skin.⁵¹ Although these findings have shed light on some effects OI- Na^+ has on its micro-environment, much remains unknown about its full implications and mechanisms. In particular, the study of OI- Na^+ storage in CKD and HD patients is currently a popular research topic.

1.4.4 Sodium (Na^+) in CKD

In the body, Na^+ content is dictated by Na^+ consumption and Na^+ excretion, which are assumed to be in equilibrium. Na^+ excretion depends on losses through sweat, the gastrointestinal tract, and mostly the kidneys. Since kidney function is compromised in patients with CKD, they have difficulties maintaining Na^+ balance in the body. This can occur due to damage to the tubule that reduces its ability to reabsorb Na^+ , or damage to the glomerulus that reduces Na^+ filtration into Bowman's capsule. The latter is most common and results in increased Na^+ retention. For this reason, patients with CKD are prescribed low salt diets and diuretics to prohibit Na^+ accumulation in the body.⁷ Diuretics work by decreasing the reabsorption of Na^+ in the tubules of the nephrons which increases the amount of Na^+ removed by the kidneys.

Since the 1980s, dialysis units have been using higher dialysate Na^+ concentrations to limit the amount of Na^+ removed in need of avoiding hypotensive conditions, disequilibrium, and discomfort for hemodialysis patients.⁵² Unfortunately, these high

concentrations of dialysate Na^+ can lead to an influx of Na^+ into the body instead of removal.⁵³ This increase in bodily Na^+ increases fluid retention, which causes hypertension, LVH, and heightened CVD risk.⁷ The accumulation of OI- Na^+ in tissue has also been found in HD patients, and is correlated with adverse outcomes.^{40,49,54}

1.4.5 Sodium and Cardiac Injury

As sodium is an essential nutrient, its imbalance can be involved in mechanisms of cardiac injury. The conventional understanding of Na^+ and cardiac injury involves increased volume and pressure. It has long been accepted that an increase in Na^+ consumption will lead to an increase in blood pressure which is detrimental to cardiac health. As OA- Na^+ in the body increases, the body retains water causing extracellular volume expansion to maintain Na^+ concentration in the body. This extracellular volume expansion increases the exerted pressure of the blood on the vessel walls, otherwise known as blood pressure. An increase in pressure and volume overload is well known to cause many cardiovascular complications such as LVH and increased risks of developing CVD.⁷

The emerging relationship between Na^+ and cardiac injury is much more complex and involves factors far beyond pressure and volume overload. Firstly, Na^+ has been found to relate to cardiac injury in indirect ways such as through cardiac ischemia, inflammation, sodium glucose co-transporter 2 (SGLT-2) inhibitors, the sodium-calcium ($\text{Na}^+/\text{Ca}^{2+}$) exchanger, extracellular volume expansion, and Na^+ deposition in distant tissues:

a) Cardiac Ischemic Reperfusion Injury

Patients on hemodialysis are prone to myocardial ischemia. Myocardial ischemia involves the restricted or reduced blood flow and oxygen to the heart muscle. Multiple dialysis treatments a week can exert stress on the cardiovascular system with repeated ischemic events and may contribute to the incidence of heart failure in these patients.^{55,56} It has been found that events of ischemia in the myocardium lead to motion reduction in the LV wall that persists even after perfusion has been restored.²⁷ This is called myocardial stunning. Repetitive episodes of ischemia-reperfusion injury

can be cumulative and eventually lead to cardiac fibrosis.⁵⁵ Modulating dialysate Na^+ concentrations has shown promise for reducing intradialytic cardiac dysfunction for patients undergoing hemodialysis treatment and potentially preventing cardiomyopathy in these patients in the future.²⁷ Beyond this, a substantial build-up of intracellular Na^+ was observed minutes after the onset of ischemia in preclinical studies on the hearts of rats and ferrets.⁵⁷⁻⁵⁹ Similarly, OI- Na^+ in the affected myocardium has been found to correlate with ischemic conditions in the hearts of humans.^{10,44}

b) Inflammation

Inflammation is an immune reaction that occurs when the body senses an injury or infection. There has been many research studies indicating that high consumption of salt can induce immune responses in the body to promote inflammation and organ damage.⁶⁰⁻⁶² Inflammation is particularly common in patients on HD, which contributes to their excess CVD risk.⁶³ It has been found that increasing the amount of Na^+ removed during dialysis can reduce inflammation in HD patients and subsequently reduce their chances of CVD events.⁶⁴

c) Sodium Glucose Co-Transporter 2 (SGLT-2) Inhibitors

The sodium glucose co-transporter 2 (SGLT-2) transports Na^+ and glucose together across the cell membrane and is important for glucose reabsorption in the nephron of the kidney. SGLT-2 inhibitors prevent the action of this transporter and therefore encourage the excretion of glucose and Na^+ from the body. There has been much research on the cardioprotective effects of these inhibitors.^{65,66} Not only have SGLT-2 inhibitors been found beneficial for heart failure patients, but they have also been found to decrease adverse cardiovascular events, slow the progression of kidney disease, and decrease overall mortality in CKD patients.⁶⁶ Some of the possible mechanisms of the SGLT-2 inhibitor positive effects include lowering blood pressure, preventing inflammation, preventing ischemia, and inhibiting the Na^+/H^+ exchanger, which would otherwise increase Na^+ myocardial levels.⁶⁷ With SGLT-2 inhibitors

identified as beneficial for CKD and heart failure patients, it is possible that decreased Na^+ excretion and increased myocardial Na^+ are involved in this comorbidity.⁶⁸

d) Sodium-Calcium ($\text{Na}^+/\text{Ca}^{2+}$) Exchanger

The sodium-calcium ($\text{Na}^+/\text{Ca}^{2+}$) exchanger is an important membrane protein that removes calcium from cells by exchanging them with Na^+ but depending on the electrochemical gradient, can also exchange in the opposite manner. It is known that elevated intracellular Na^+ is present in human failing myocardium.⁶⁹ These increases in intracellular Na^+ can cause increased intracellular calcium through the work of the $\text{Na}^+/\text{Ca}^{2+}$ exchanger. Remembering the importance of the calcium ion in myocyte contractility, the increase of intracellular calcium can contribute to arrhythmia and cardiac dysfunction.⁷⁰

e) Extracellular Volume Expansion

During dialysis, much stress is placed on the cardiovascular system, which includes intradialytic hypotension, ischemia, and the build-up of uremic toxins.^{30,71} These stresses cause cumulative damage during dialysis which can result in the death of cardiomyocytes and edema. What is left is a larger extracellular to intracellular volume ratio in tissue. Since there is a higher concentration of Na^+ in the extracellular fluid, the Na^+ content in this region may reflect this extracellular fluid volume expansion. Studies by Rossitto et al. have predicted this phenomenon.^{72,73} In general, HD patients are known for having extracellular fluid volume expansion.^{53,74} This expansion of extracellular fluid is one of the factors that contributes to LVH which we know is detrimental to heart health.³⁰

f) Sodium Deposition in Distant Tissues

OI- Na^+ deposition has been found to occur in many tissues in the body, such as skin, bone, and muscle.⁴⁹ An abundance of preclinical data suggest that OI- Na^+ tissue deposition may cause a chronic inflammatory state of the body and tissue remodeling. In humans, the skin is known to be a major Na^+ reservoir, creating an extracellular volume expansion buffer as excess Na^+ in the body is stored without water.⁵⁰ A study

by M. Schneider et al. discovered that skin Na^+ concentration correlates with LVH in patients with CKD.⁴⁰ It has also been found that humans with severe heart failure have very high levels of OI- Na^+ storage in the skin.⁷⁵ Studies such as these suggest Na^+ is linked with cardiac injury, especially in patients with CKD that have high cardiovascular risk.^{49,76} Although, the mechanisms at play remain unclear.

Secondly, preclinical studies have shown a direct relationship between Na^+ and cardiac injury, suggesting Na^+ may be deposited in the myocardium leading to tissue remodeling.⁷⁷ A study by Yu et al. examined the effects of increased dietary salt on fibrosis in normotensive and hypertensive rats. It was found that myocardial Na^+ deposition induces myocardial fibrosis in rats independent of hypertension.¹¹ One of the main aims of our future work is to determine whether this relationship between myocardial Na^+ deposition and cardiac fibrosis may be occurring in humans as well.

1.5 Magnetic Resonance Imaging (MRI)

MRI is a non-invasive diagnostic imaging tool that uses strong magnetic fields to produce detailed anatomical images of the human body. To produce the images, it takes advantage of the magnetic properties of nuclei in the human body. These 3-dimensional images can then be analyzed for tissue pathologies and therefore help diagnose and treat various medical conditions.

There are three main components in an MR scanner that work together to produce the images: the main magnet, the radiofrequency (RF) coils, and the gradient coils. During an MRI scan, the patient is placed inside the bore of the MRI machine (Figure 1.11), where there is a strong and uniform magnetic field of strength 1.5-3 T for clinical scanners or 7-11.7 T for pre-clinical scanners. Many nuclei (including H^+ and Na^+) possess a magnetic dipole moment. When a patient is placed in the MR scanner, these nuclear dipole moments in the tissue precess around the direction of the main magnetic field (B_0). The distribution of precessing moment is slightly skewed in the direction of B_0 , giving rise to a net magnetization (M) of the tissue in this direction (Figure 1.12a). An RF pulse is then given to the body in the form of a radio wave, which tips the magnetization M away from the direction of the B_0 (Figure 1.12b). This causes the bulk magnetization to precess

around B_0 . As the magnetization precesses it quickly returns to its equilibrium direction, simultaneously inducing a small voltage in a receiver coil which is the detectable signal for MRI. (Figure 1.12c).

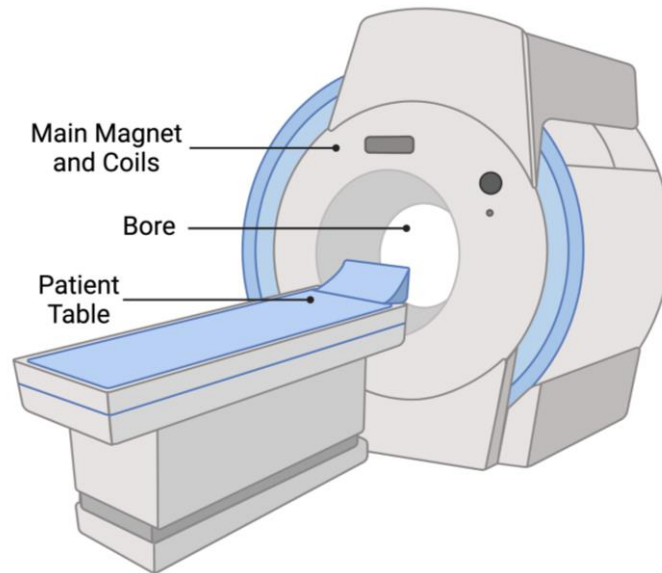


Figure 1.11: Labeled diagram of an MRI machine, including the bore, main magnet and coils, and patient table. Created in BioRender.com.

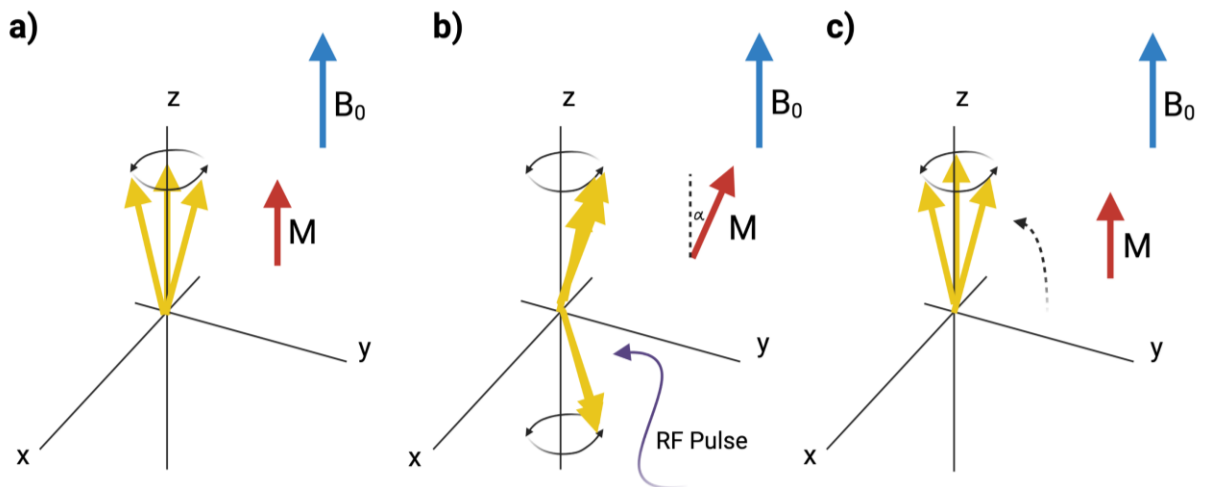


Figure 1.12: Magnetization of nuclei a) while aligned with main magnetic field, b) immediately after an RF pulse, and c) after relaxation back to direction of main magnetic field. Direction of net magnetization (M) and main magnetic field (B_0) indicated at each step. Created with BioRender.com.

There are two directions in which the relaxation of the magnetization is measured: longitudinal and transverse. The longitudinal relaxation, also known as the spin-lattice relaxation, quantifies the recovery of the longitudinal component of the magnetization along B_0 . The time it takes to recover 63% of the equilibrium magnetization is referred to as the T1 (spin-lattice relaxation) time (Figure 1.13a). The transverse relaxation, also known as the spin-spin relaxation, explains the dephasing of spins by the transfer of energy between neighboring nuclei. This transverse or spin-spin relaxation is characterized by a time constant, T2, which represents the time it takes until only 37% of nuclei spins are still in phase (Figure 1.13b). These T1 and T2 times vary between tissue types.

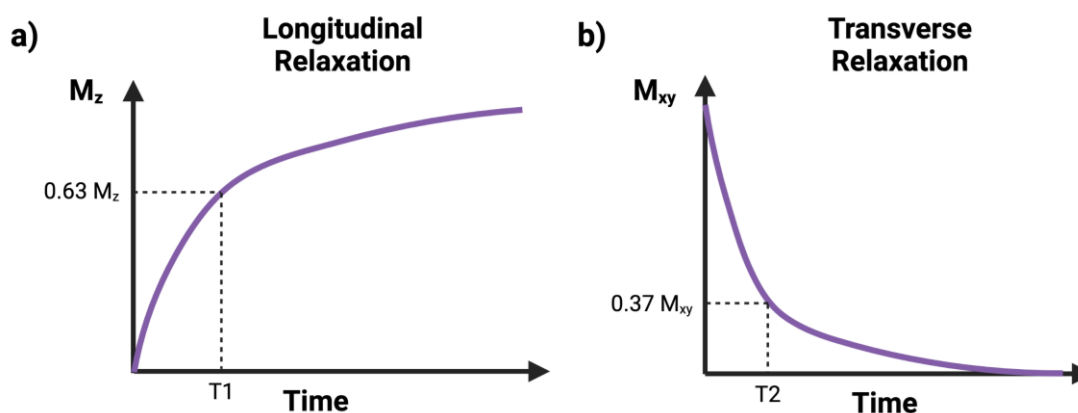


Figure 1.13: Graphical representation of the a) longitudinal relaxation and b) transverse relaxation of nuclei after an RF pulse. T1 and T2 times indicated on graph. Created with BioRender.com.

To attribute the detection of signal to a certain location in the body and produce sets of 2-dimensional images, the gradient coils are used. There are gradient coils for the x, y, and z directions. These gradient coils produce a secondary magnetic field that alters the main magnetic field as a function of position along each gradient direction. This allows for spatial encoding of the MR signal.⁷⁸

1.5.1 Pulse Sequences

To acquire images using MRI, the RF pulses and the gradients must be applied to the tissue in a specific sequence. This sequence must allow for the change in nuclei

magnetization, slice selection, and spatial localization, and this must be repeated many times to obtain multiple images. The order, strength, and duration of these gradients as well as the type of RF pulse can be specified depending on the image information and signal-to-noise ratio (SNR) desired. These unique sequences of applications of gradients and RF pulses are referred to as pulse sequences. These pulse sequences have specific parameters by which they are defined. A few of these parameters are:

- 1) Echo time (TE): the time it takes to receive a signal after the administration of the RF pulse.
- 2) Repetition time (TR): the time between the start of the pulse sequence and when it is repeated.
- 3) Flip angle (α): the angle of which the longitudinal magnetization is tipped into the transverse (xy) plane.

Pulse sequences are also instructions on how to record the signal produced from tissue in the 2-dimensional spatial frequency domain called k-space. K-space contains low spatial frequencies in the center of the domain and high spatial frequencies in the periphery. It is then this frequency domain that gets converted to the spatial domain (the anatomical image) through a mathematical operation called the Fourier transform.

The main pulse sequences used in this thesis produce images that are nuclear density weighted. Nuclear density weighted images have signal intensity values that relate to the number of nuclei in the area being imaged, therefore T1 and T2 weighting are both minimized. These types of imaging sequences use long TRs and short TEs to achieve this effect. Applications of these sequences include quantification or comparing relative amounts of nuclei in specific anatomical regions between individuals.

1.5.2 Proton (H^+) MRI

In theory, nuclei with an odd number of protons or neutrons can be imaged with MRI because they have net nuclear spin and dipole moment. This includes nuclei such as H^+ ,

Na^+ , ^{19}F , and ^{13}C . Nuclei with an even number of protons and neutrons cannot be imaged with MRI.

H^+ nuclei have a net nuclear spin of $\frac{1}{2}$. H^+ nuclei are the most common nuclei used for MRI because of their high abundance in tissue and their magnetic properties. H^+ has the largest gyromagnetic ratio of all nuclei, with a value of 42.58 MHz/T. The gyromagnetic ratio is the ratio of a nuclei's magnetic moment to its angular momentum. The larger the nuclei's gyromagnetic ratio, the higher its MR sensitivity.

For the MR scanner to specifically image the H^+ nuclei, it needs to be tuned to excite only the H^+ nuclei. This is done by using an RF coil that is tuned for the specific Larmor frequency (ω_0) of the nuclei of interest, in units of megahertz. The Larmor frequency depends on the magnetic field strength (B_0) in units of tesla and the nuclei's intrinsic gyromagnetic ratio (γ) in units of megahertz per tesla, and is calculated using the following equation:

$$\omega_0 = \gamma B_0 \quad [1.5]$$

1.5.2.1 Cardiovascular Magnetic Resonance (CMR)

Cardiovascular magnetic resonance (CMR) is a medical imaging technique that can non-invasively assess the structure and function of the heart by imaging the organ with MRI. For this reason, CMR is a diagnostic tool that can distinguish cardiac health from disease.³⁹ Cardiac structure and function are assessed using CMR by measuring specific cardiac parameters from the images. These parameters include LVM, LV ejection fraction (LVEF), EDV, ESV, and SV. Table 1.2 provides definitions and units for these parameters, and the research paper by J. Schulz-Menger et al. provides more information on measuring them.⁷⁹

Table 1.2: Parameters for Assessing Cardiac Function

	Units	Definition
Left Ventricular Mass (LVM)	Grams (g)	Weight of the left ventricle.
Left Ventricular Ejection Fraction (LVEF)	Percent (%)	Percentage of blood in the left ventricle at the end of diastole that gets pumped out of the left ventricle during one systolic contraction.
End Diastolic Volume (EDV)	Milliliters (mL)	Volume of blood in the left ventricle at the end of diastole/ventricular filling.
End Systolic Volume (ESV)	Milliliters (mL)	Volume of blood in the left ventricle at the end of systole/ventricular contraction.
Stroke Volume (SV)	Milliliters (mL)	Volume of blood pumped out of the left ventricle during one systolic contraction.

For CMR imaging, the conventional MRI sequences must be adjusted. This includes ECG gating to account for the movement of the heart during image acquisition and breath-holds to minimize motion from breathing. The typical technique used to acquire CMR images is cine imaging. Cine imaging is used to capture cardiac motion by synchronizing the signal acquisition to the cardiac cycle using an ECG. Cine images are collected at different slices of the heart. For each slice, data is acquired continuously and then separated into very short windows of time along the entire cardiac cycle. The data in each of the sections is reconstructed into separate images which is referred to as retrospective gating. Afterwards, the images along the cardiac cycle can be combined to produce cardiac cine MRI.⁷⁸

1.5.3 Sodium (Na^+) MRI

MRI can also be adapted to detect Na^+ nuclei. This can be done by using a custom RF coil tuned for the specific Na^+ Larmor frequency. Na^+ is the second-most MR visible nucleus present in the human body due to its concentration in tissue and its natural stable isotopic abundance of 100%.⁴⁵ Although, Na^+ MRI is challenging because of its lower sensitivity, which is about 1/11 the sensitivity of H^+ .⁸ This is mainly due to the gyromagnetic ratio of Na^+ , which is 11.26 MHz/T. Additionally, Na^+ has a net nuclear spin of 3/2, giving Na^+ a quadrupolar moment. Compared with H^+ , this causes faster spin-lattice and spin-spin relaxation. The latter having a biexponential signal decay with a fast and short component in human tissue.⁴⁵ As a result, faster imaging must occur during Na^+ MRI due to this rapid decay of signal. Na^+ MRI is also known for having a very low SNR, therefore imaging parameters must be adjusted to optimally image the Na^+ nuclei.

1.5.3.1 Density Adapted 2D Projection Reconstruction (DA2DPR) Pulse Sequence

A pulse sequence that has been successfully demonstrated for Na^+ MRI and the pulse sequence used in this thesis is the density adapted 2D projection reconstruction (DA2DPR) pulse sequence.^{80,81} This sequence was optimized for implementation on a 3-T MR scanner, producing an ultrashort TE of 1.2ms, a TR of 100ms, and a flip angle of 90° . The values of these parameters produce an imaging contrast that is proportional to tissue sodium concentration. Since transverse relaxation is very fast for Na^+ , the TE must be ultra-short to measure signal from the tissue before it decays after excitation. The TR is chosen to be long enough to allow the longitudinal magnetization to recover before repeating the pulse sequence, this allows for a strong signal from all Na^+ nuclei. Lastly, the flip angle is 90° to tip the entire longitudinal magnetization into the transverse (xy) plane to get the maximum signal per RF excitation pulse.

The DA2DPR pulse sequence is unique because it acquires k-space using radial trajectories, starting from the center, and reaching out to the periphery of k-space. Along each trajectory there is density adaption that ensures uniform k-space sampling to account for the radial trajectories getting further apart from one another towards the periphery of

k-space (Figure 1.14). This way, the higher and lower spatial frequencies are evenly sampled which avoids blurring and SNR loss in the resulting images.

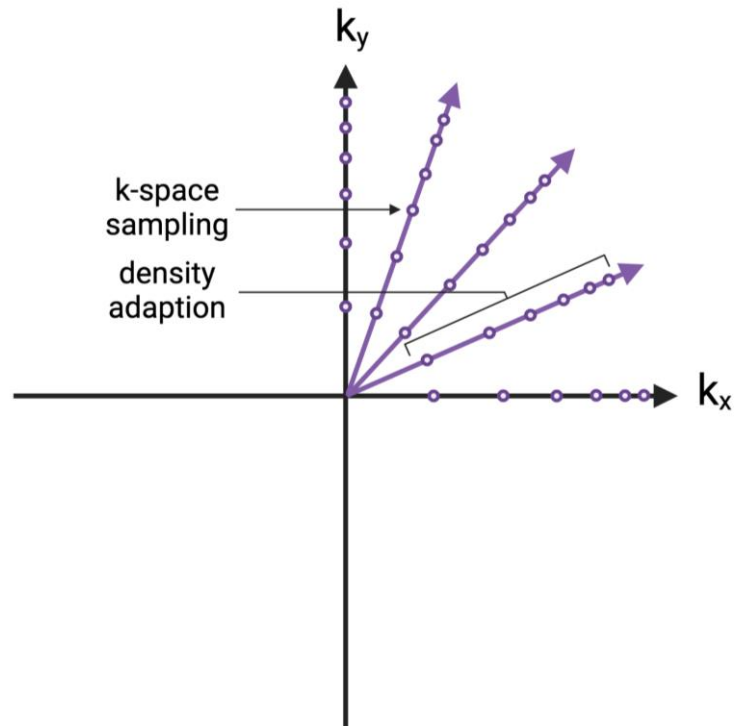


Figure 1.14: Graphical representation of k-space with radial trajectories for image acquisition with DA2DPR pulse sequence. Spheres indicate k-space samples that are closer together towards the end of trajectories to proportionately sample k-space.

Created with BioRender.com.

1.5.3.2 Sodium (Na^+) MRI Applications

Some of the earliest research with Na^+ MRI began in the early 1980's.^{43,82} Since Na^+ MRI images the Na^+ nuclei, it can provide different information than conventional H^+ MRI. Na^+ MRI can detect local changes in Na^+ concentration which are altered by disease. For this reason, Na^+ MRI has been used to non-invasively study the manifestation of many diseases and evaluate therapies. Some of the diseases assessed by Na^+ MRI include diabetes, multiple sclerosis, osteoarthritis, kidney disease, and cancer in response to chemotherapy.^{45,83}

Most relevant to this thesis, Na⁺ MRI of the human heart has been used to study myocardial infarction, Conn's syndrome, and Na⁺ content of the healthy myocardium. It has been found that Na⁺ content of the human myocardium is elevated in myocardial infarction which has been measured using signal intensities and absolute quantification of sodium concentration.^{10,44} Myocardial Na⁺ content was also found to be elevated in patients with Conn's syndrome in comparison to controls using a ratio of tissue Na⁺ intensity to the intensity of a 100mM reference vial.⁸⁴ This study by Christa et al. suggests that the myocardium may be a novel site of Na⁺ storage. To mention for reference, a few studies have found the myocardial Na⁺ content in the septum of healthy individuals to be around 52 mM.^{85,86} This thesis will now attempt to prepare the imaging protocol for future studies evaluating the myocardial Na⁺ content of the septum in CKD patients and controls using cardiac Na⁺ MRI.

1.5.4 Radiofrequency (RF) Coils

As mentioned previously, RF coils are needed to transmit RF pulses at the Larmor frequency to excite the nuclei and receive the resulting signal. These RF coils can be specifically for transmitting, receiving, or both. There are many different types of RF coils, and each of them can be tailored to the anatomical region being imaged. The most common type of RF coil used for transmission is the built-in body coil surrounding the entire patient which is used exclusively for proton imaging. As for receiver coils, there are two types; volume coils and surface coils.⁷⁸

1.5.4.1 Surface Coils

Surface coils are typically small receive-only RF coils that are placed on the surface of the patient, over the anatomical area being imaged. Some of the advantages of surface coils include that they are simple to manufacture in comparison to other coils and have a high sensitivity near their surfaces. For this reason, they are often used for imaging superficial structures. Surface coils are less desirable for imaging deeper anatomical structures because their sensitivity decreases significantly with depth.⁷⁸ Therefore, there is a nonuniform signal intensity distribution in the resulting image.

To overcome this disadvantage, the sensitivity must be corrected. Intensity correction allows the proper display of intensity and the quantitative assessment of surface coil images. Axel et al. describes methods to help obtain uniform image intensity over a region of interest imaged using a surface coil.⁸⁷ There are two methods in which the intensity correction can be performed: using an additional image of a phantom or using the blurred original image. To save time and to avoid image co-registration, the blurred image method can be used, but using an image of a phantom allows for a more accurate intensity correction. In general, the image of the desired object is acquired, and an image of a uniform phantom. A uniform phantom refers to a reference object with uniform and known imaging properties that is used to mimic tissue, and in this thesis, it is a container filled with 150mM of sodium chloride dissolved in water. The phantom image is then normalized (the image signal intensities are scaled to be between zero and one) and divided into the image of the object. This proportionately increases the signal in the areas of the image that are further away from the coil to compensate for the intensity drop-off. These methods will be applied in this thesis to our surface coil Na⁺ MR images to allow for relative assessment of the Na⁺ signal.

1.6 Objectives and Hypotheses

This thesis involves technical adaptations of Na⁺ MRI to image the cardiac tissue of healthy participants. The objectives of this research are: 1) To determine the effect of ECG gating on Na⁺ MR image quality, and 2) To develop a pipeline to correct cardiac Na⁺ MR images for non-uniform surface coil spatial sensitivity. The hypotheses are: 1) ECG gating will improve Na⁺ MR image quality, and 2) the signal intensity of Na⁺ MR images acquired with a surface coil will be made uniform with the use of phantom images for improved quantification of tissue sodium concentration. Chapter 2 examines the effect of ECG gating on Na⁺ MR image quality.

Chapter 2

2 The Effects of ECG Gating on Na⁺ MR Image Quality

This chapter contains a technical analysis of the effects of ECG gating on Na⁺ MR image quality with a condensed introduction (background, objectives, and hypotheses), methodology, results, and discussion. This study was conducted preliminary to the main study of this thesis presented in chapter 3 and was intended to be applied to future patient studies.

2.1 Introduction

2.1.1 Sodium (Na⁺) in the Body

The sodium (Na⁺) ion is the most abundant cation in the human body. Its presence is vital for inducing muscle contraction, transmitting nerve impulse, maintaining homeostasis, and more. Separated by the cell's semi-permeable membrane, the Na⁺ concentration surrounding the cell is found to be 140-150mM in comparison to the intracellular concentration of 10-15mM. This concentration difference is maintained by the sodium-potassium pump, which consumes energy in the form of adenosine triphosphate to transport these ions through the cell membrane. However, there are many mechanisms that can affect this concentration difference. The proper balance of intra vs extracellular Na⁺ is a measure of cell membrane integrity. Pathological changes such as the impairment of the sodium-potassium pump, as well as edema, tissue injury, or necrosis may lead to an increase in the Na⁺ concentration in tissue. Therefore, tissue Na⁺ concentrations can be indicative of disease.^{43,54}

2.1.2 Sodium (Na⁺) MR Imaging & Applications

With Na⁺ as the second most visible nucleus with nuclear magnetic resonance, Na⁺ magnetic resonance imaging (MRI) can be used to non-invasively assess Na⁺ concentrations in the human body. As serum sodium measurements assess the electrolyte balance of the entire blood pool, measurements of in vivo Na⁺ levels can provide

specialized information of sodium content in specific regions. This becomes useful when investigating diseases that result in a disruption of Na^+ concentrations. These disease conditions include kidney failure, osteoarthritis, diabetes, hypertension, myocardial infarction, and more.^{45,83}

A specific region of the body warranting further investigation of changes in tissue Na^+ concentration is the myocardium. Increased Na^+ levels in the human myocardium may indicate ischemic disease, myocardial infarction, edema, loss of cell membrane integrity, and more.⁸ Cardiac Na^+ MRI can be used to assess myocardium Na^+ levels, but this type of imaging also brings forth unique challenges.

2.1.3 Challenges of Cardiac Sodium (Na^+) MRI

Na^+ may be the second-best nucleus to detect using MRI, but obtaining good quality images remains challenging due to the lower tissue concentration, MR sensitivity, and gyromagnetic ratio of Na^+ in comparison to the conventional H^+ .⁸ This alone reduces the SNR and resolution in the resulting images. With cardiac Na^+ MRI, once you consider the movement of the heart and lungs, obtaining quality images becomes more difficult. Some of the most recent studies using cardiac Na^+ MRI reported an SNR of 26 ± 2 in the myocardium and a resolution of $(6 \times 6 \times 6) \text{ mm}^3$.⁸⁸ It is thought that using ECG gating with cardiac Na^+ MRI would result in a higher SNR.⁸⁰ However, in a study by Lott et al. the SNR of images that were sorted by cardiac motion were found to be lower than the non-sorted images.⁸⁶

2.1.4 Cardiac Sodium (Na^+) MR ECG Gating

Retrospective gating is typically used for acquisition of cardiac Na^+ MRI. This involves continuous imaging with simultaneous acquisition of ECG data. Post imaging, only image frames of the heart acquired during diastole are averaged and omits those acquired during systole to create the final image. This reduces motion artefact in the final averaged image. This strategy is considered to be the least SNR-costly method as it allows for continuous data acquisition.^{8,80} Since cardiac Na^+ MRI is a less common field of research, ECG gating for sodium imaging hasn't been widely investigated. Much of the

research that has been undertaken on this topic is associated with 7-T scanners, which are less clinically applicable; access to a 3-T scanner is far more typical.^{86,89,90} Regardless of the field strength, the results from these studies demonstrated differences in measurement of the myocardium Na⁺ signal of no more than 5% between ECG gated and non-gated images.^{80,86}

2.1.5 Objective and Hypothesis

The objective of this study is to determine whether cardiac gating of Na⁺ MR images improves image quality by comparing retrospectively gated images to non-gated images. This is important to determine for future studies that wish to quantify cardiac sodium concentrations from Na⁺ MR images. Considering Na⁺ MRI has an intrinsically low signal-to-noise ratio (SNR), we investigated changes to the point spread function (PSF), SNR, and geometric distortion between the two image groups. Previous studies have also been conducted to assess MR image quality with resolution, SNR, and geometric distortion.⁹¹⁻⁹³ The PSF is a measure of the spatial resolution of the imaging system using the full width at half-maximum (FWHM) of its peak. Spatial resolution is an important metric because it represents the smallest feature that can be resolved in the image. SNR is another important imaging parameter that measures the amount of signal present in the image in comparison to the amount of background noise or signal fluctuations. SNR is therefore a measure of image quality. Lastly, geometric distortion can be a measure of image artefact. This can be done in the cardiac Na⁺ MR images by measuring the septum thickness to determine whether the ECG gated and non-gated images exhibit differences in anatomical length measurements. Overall, it is hypothesized that cardiac Na⁺ ECG gating will remove any geometrical distortion, maintain spatial resolution, but reduce SNR. This is because cardiac motion will be removed from image acquisition, but this omitted data will also reduce the amount of signal collected.

2.2 Methodology

2.2.1 Study Design

This was a cross-sectional pilot study. During one study visit, each participant provided demographic information before H^+ and Na^+ MRI scans of the heart were acquired.

This study was approved by the University of Western Ontario Health Sciences Research Ethics Board before any study visits took place. The entirety of this study was conducted in accordance with the approved protocol and Good Clinical Practice Guidelines.

2.2.2 Participants

The four study participants were recruited from London, Ontario, Canada. Participants with a previous history of cardiovascular disease or those who did not pass the facility screening form were excluded from this study prior to written informed consent. Age of participants ranged from 35 to 48 years.

2.2.3 H^+ and Na^+ MR Acquisition

All H^+ and Na^+ MR image data were acquired using a 3.0-T MRI machine (Discovery MR750, General Electric Healthcare, Milwaukee, WI, USA). Participants were positioned supine and feet-first within the magnet bore.

Cardiac Na^+ MR images were acquired using a custom-built two-loop (18cm diameter) butterfly radiofrequency surface coil tuned for Na^+ frequency (33.786 MHz). The coil was placed around the chest and centred over the heart, with one loop on the anterior and one loop on the posterior side of the body. The coil location was adjusted to ensure the heart was placed in the centre of the two loops using proton anatomical images obtained by the MRI built-in body coil which include fiducial markers incorporated into the RF coil. A density-adapted 2-dimensional projection reconstruction pulse sequence for Na^+ MRI was implemented with the following parameters: FOV = $36 \times 36\text{cm}^2$, in-plane resolution = $0.3 \times 0.3\text{cm}^2$, slice thickness = 3cm, TR = 100ms, TE = 1.2ms, flip angle = 90 degrees, signal averages = 50, radial projections = 378, acquisition time = 31.5 minutes. The slice prescribed was a mid-short-axis slice of each participant's heart.

Simultaneous ECG data were also acquired during each scan using electrodes placed on the chest, and the images were acquired while the participant was free breathing.

Cardiac H^+ MR images were obtained using the built-in RF body coil. Short-axis images covering the entire left ventricle were acquired using a 2D CINE fast imaging employing steady state acquisition (FIESTA) pulse sequence with an 8-mm slice thickness, 2-mm slice gap, 36 x 36-cm² field of view, 224 x 224 matrix, 3.5-ms repetition time, 1.5-ms echo time, 45-degree flip angle, 69-ms temporal resolution, 1.6 x 1.6 mm² in-plane image resolution, and 125kHz bandwidth. Breath holds and prospective ECG triggering were used during the scan to gate the images. Sets of 25 images were collected across the cardiac cycle for each slice. Number of slices and acquisition times varied between participants as they depended on heart length and heart rate.

2.2.4 Data Analysis

The Na^+ MR raw k-space data was reconstructed into four mid-short axis Na^+ MR images for each participant with a 2048x2048 matrix in MATLAB (Mathworks, R2020a, Natick, MA) using a non-uniform fast Fourier transform. The four Na^+ MR images were retrospectively gated to contain data from 25%, 50% 75% and 100% of the cardiac cycle as shown in figure 2.1.

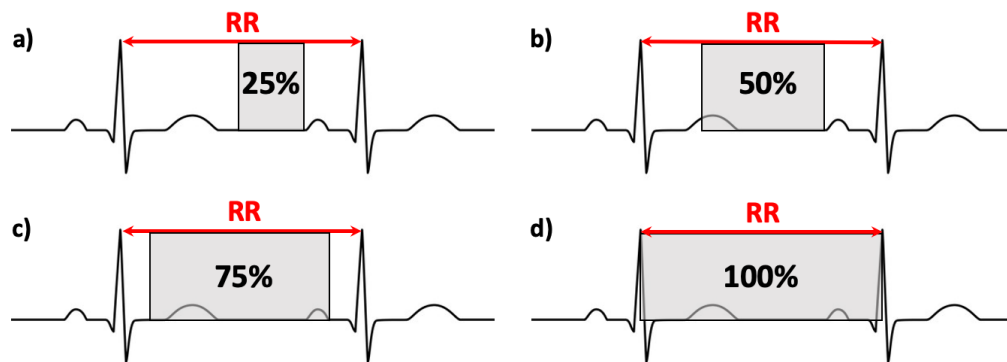


Figure 2.1: Visual representation of the regions of the cardiac cycle during which data was collected for the images containing a) 25%, b) 50%, c) 75%, and d) 100% of data from the cardiac cycle. The R-R interval here represents one full cardiac cycle.

In MATLAB, the mid-short axis H^+ MR images were used to create two H^+ MR images for each participant with a 2048x2048 matrix. The first was an average of all 25 images (100% of the cardiac cycle), and the second was an average of the 14 images where the ventricles were found to be in resting position (56% of cardiac cycle).

For the point spread function analysis, a simulation was used to represent the signal of a 3mm ideal object based on participant k-space image data. The object's k-space data was modified depending on the amount of data that was used to reconstruct each participant's gated and non-gated images (using 25%, 50% and 100% of their cardiac cycles). This was performed in MATLAB using an inverse Fourier transform and a Fourier transform. The resulting point spread functions were overlaid on one graph for comparison.

For the signal-to-noise ratio (SNR) measurements, regions of interest (ROIs) were drawn around the right ventricle, left ventricle, septum, skin, and a small region of background in each of the four Na^+ MR images for each participant. The H^+ MR images were used to guide the drawing of the ROIs on the Na^+ MR images. The mean signals and standard deviations were extracted from each of the ROIs and used to calculate the SNR with the following equation:

$$SNR = \frac{\text{mean signal}}{\text{standard deviation of background signal}} \quad [2.1]$$

In MATLAB, the SNR measurements were plotted on the same graph for each participant. The SNR measurements for the right ventricle, left ventricle, septum, and skin were separately fit to a square root curve to represent the following association:

$$SNR \propto \sqrt{\# \text{ samples}} \quad [2.2]$$

The geometrical distortion of the images was assessed by measuring the septum thickness in each of the H^+ and Na^+ MR images. In MATLAB, 18 line profiles were drawn perpendicularly across the septum in order to cover a 3mm width, which was the original resolution of the Na^+ MR images (Figure 2.2a and 2.3a). The signal intensity was

extracted at each point across each of the line profiles, and they were averaged to create one line profile for each image that was plotted on a graph of signal intensity versus pixel number (Figure 2.4 and 2.5). The same method was repeated to create a second line profile perpendicularly across a separate region of the septum that was oriented at a 45-degree angle with respect to the image orientation (Figure 2.2b and 2.3b). Using the line profiles, the pixel width was calculated at the full width at half minimum with respect to the closest local maximum in the H^+ and Na^+ images (Figure 2.4b and 2.5b) The septum thickness at both regions in each image were then calculated according to the following equation:

$$\text{Septum Thickness} = \# \text{ pixels wide} \times \text{dimension of each pixel} \quad [2.3]$$

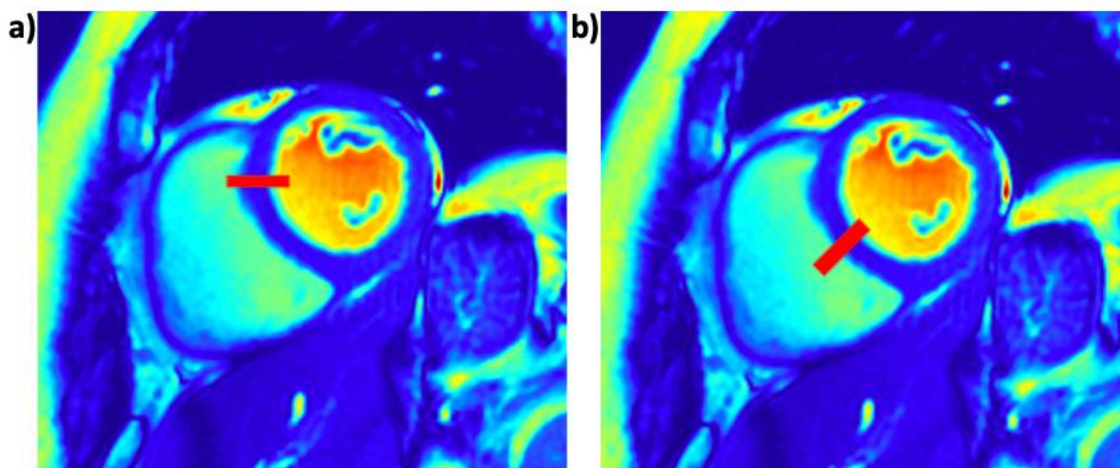


Figure 2.2: Short-axis H^+ MR images of one participant's heart depicting the line profile location oriented a) horizontally and b) at a 45-degree angle.

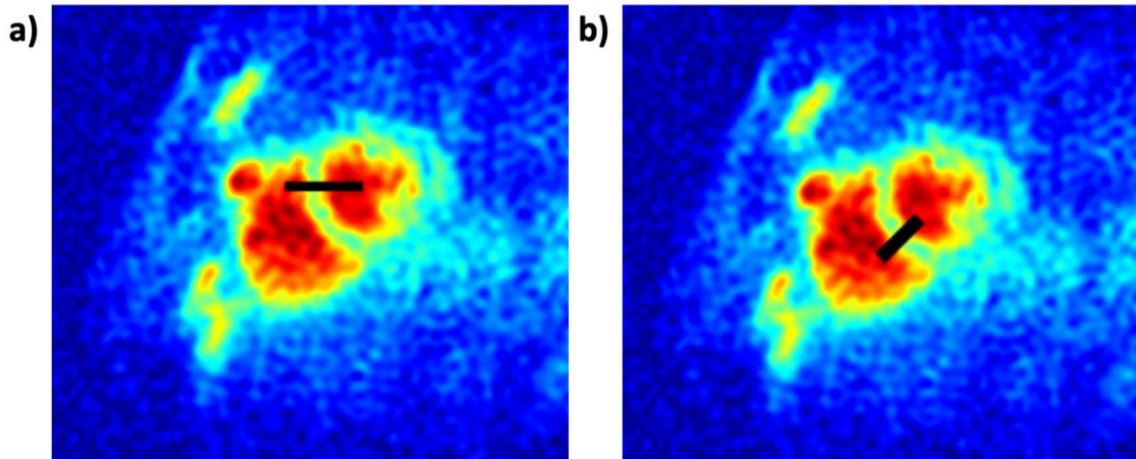


Figure 2.3: Short-axis Na^+ MR images of one participant's heart depicting the line profile location oriented a) horizontally and b) at a 45-degree angle.

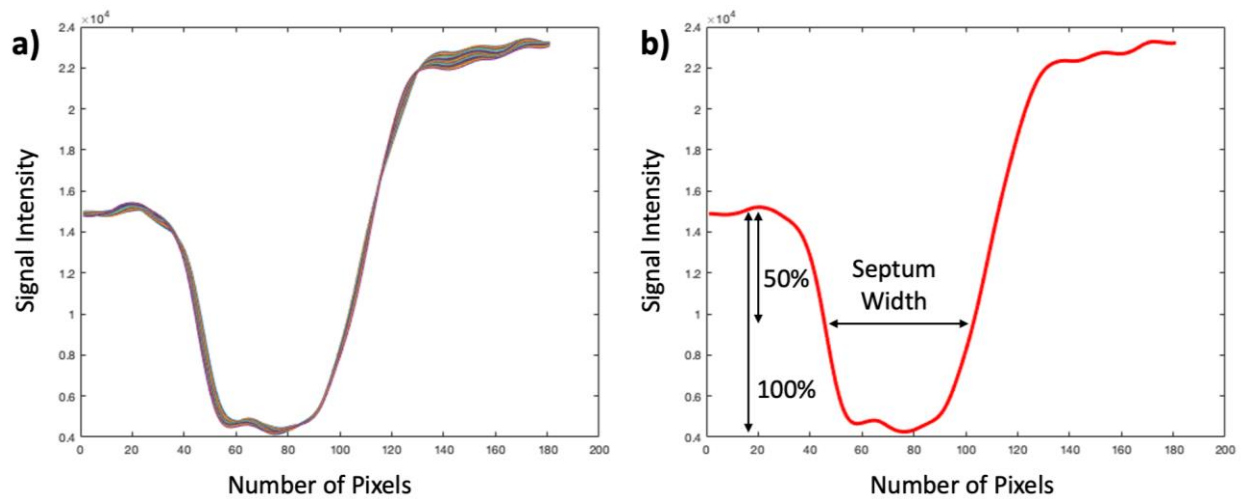


Figure 2.4: Plot showing the a) 18 line profiles and b) one average line profile across the septum in a horizontal direction for one participant's H^+ MR image before gating. The measured septum width is shown at full width half minimum with respect to the closest local maximum.

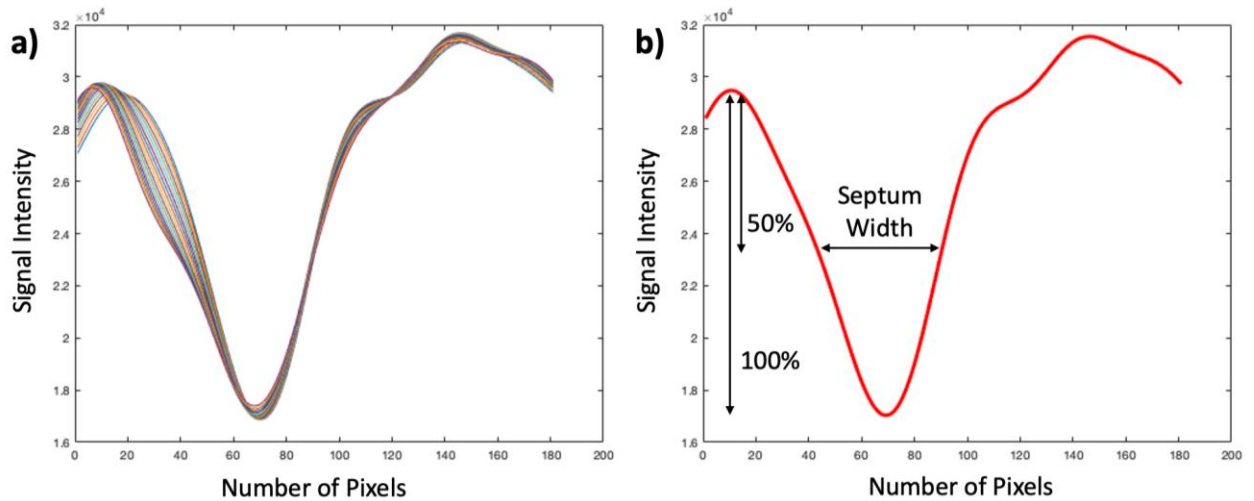


Figure 2.5: Plot showing the a) 18 line profiles and b) one average line profile across the septum in a horizontal direction for one participant's Na^+ MR image before gating. The measured septum width is shown at full width half minimum with respect to the closest local maximum.

2.3 Results

The following sections describe the results of the PSF, SNR, and geometrical distortion analysis of the reconstructed images. Figure 2.6 shows the visual differences between sodium images of a participant reconstructed using different amounts of cardiac data.

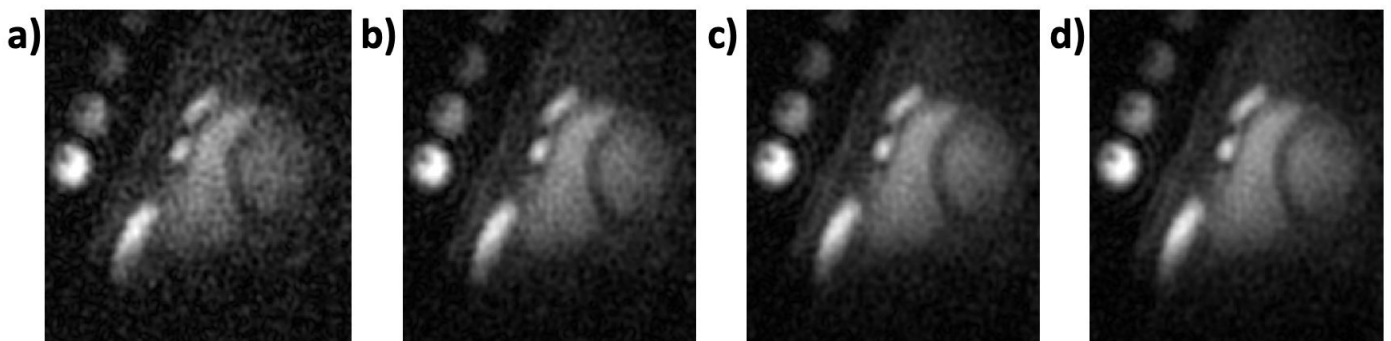


Figure 2.6: Sodium images from one participant reconstructed using a) 25%, b) 50%, c) 75%, and d) 100% of data from the cardiac cycle.

2.3.1 Measuring the Point Spread Function (PSF)

Figure 2.7 shows PSFs of an ideal object that were reconstructed using different amounts of k-space data. The amount of k-space data used for the reconstruction was based on each participant's gated and non-gated images (using 25%, 50% and 100% of their cardiac cycles). Figure 2.8 shows each of these PSFs superimposed on one another. For each participant, there was an increase in signal fluctuations surrounding the PSF the further the images were gated and for the less data they contained from the cardiac cycle. Although, when PSFs of the same participant were plotted on the same graph (figure 2.8), the FWHMs of each PSF were identical.

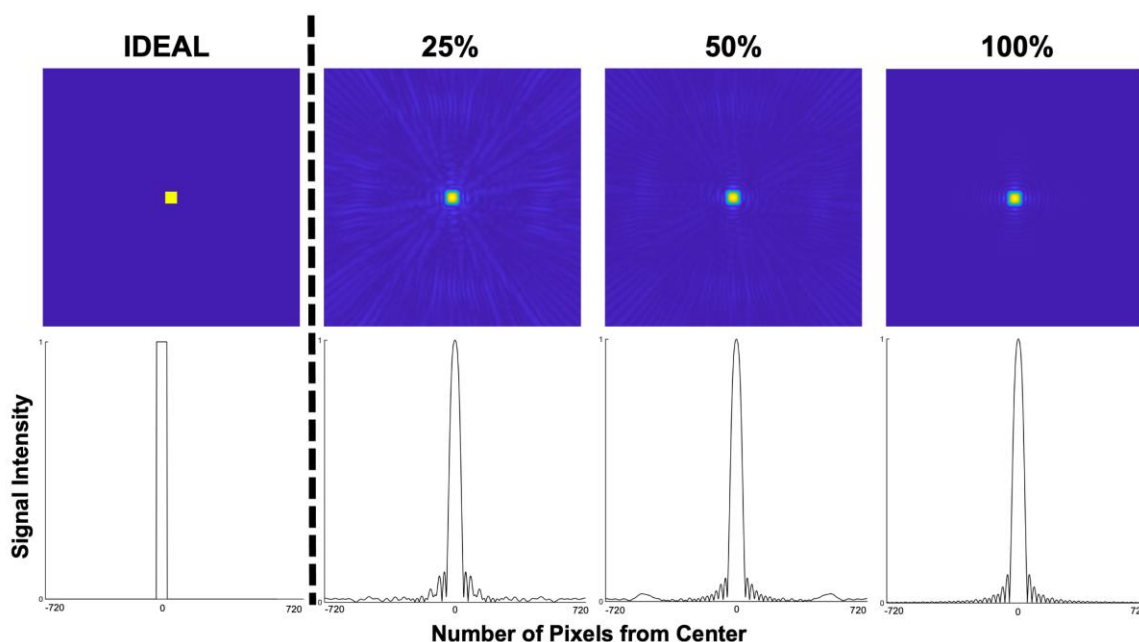


Figure 2.7: Visual representation of an isolated pixel with its corresponding point spread function (PSF) for an ideal image and images containing 25%, 50%, and 100% of data from the cardiac cycle for one participant. The PSF represents signal intensity vs distance from the center of the pixel. One pixel is 3mm wide.

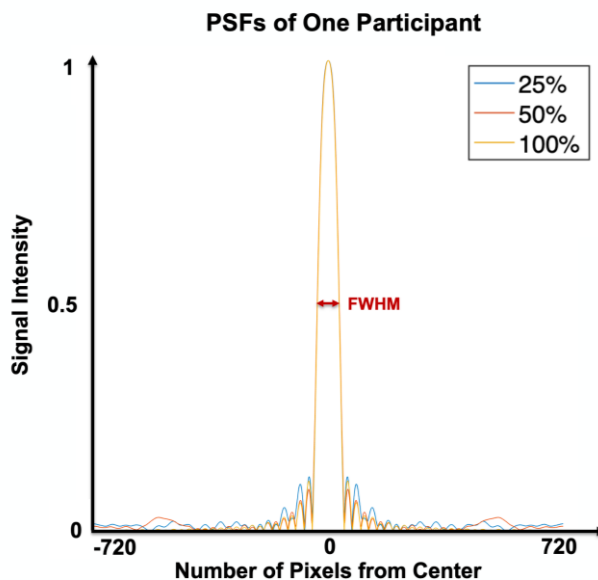


Figure 2.8: Point spread functions (PSFs) of pixels from images containing 25% (blue), 50% (red), and 100% (yellow) of the cardiac cycle of one participant plotted on the same graph. The PSFs represent signal intensity vs distance from the center of the pixel. The full-width-at-half-max (FWHM) for all PSFs is positioned on the graph. One pixel is 3mm wide.

2.3.2 Measuring the Signal-to-Noise Ratio (SNR)

The average SNR measurements of the left ventricle, right ventricle, septum, and skin were plotted against the percent of the cardiac cycle sampled for all participants (figure 2.9). Each tissue type was separately fit to a square root curve, resulting in an R^2 of 0.9866 and above. For each individual participant, the images that were gated further were found to have decreased SNR. This finding was consistent across all participants and is displayed in figure 2.9.

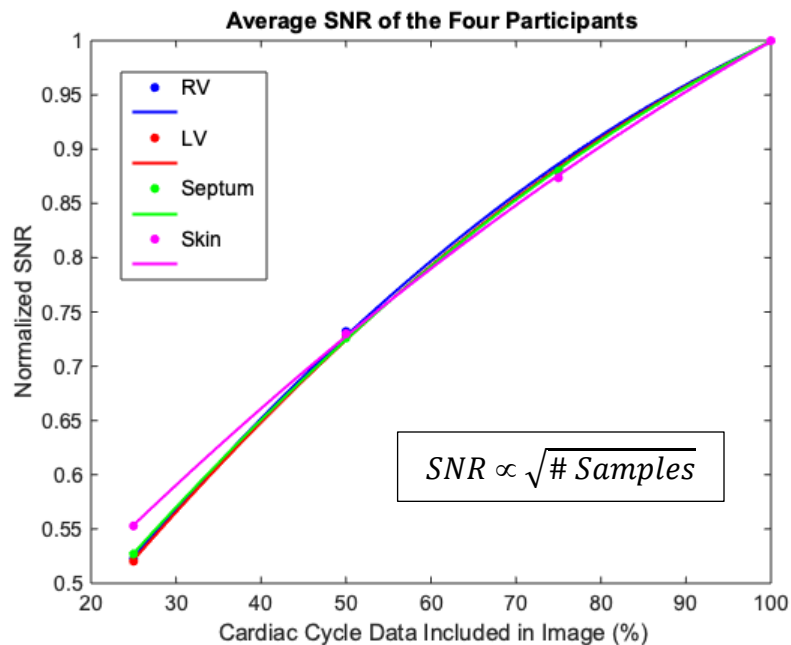


Figure 2.9: Participant mean SNR for each tissue type separated by the percent of the cardiac cycle data sampled in the image. A square root function was fit to the data for the RV ($R^2=0.9990$), LV ($R^2=0.9995$), septum ($R^2=0.9998$), and skin ($R^2=0.9995$).

2.3.3 Measuring the Geometrical Distortion

Geometrical distortion assessed by septum thickness measurements from each participant's Na^+ images are displayed in Table 2.1. Septum thickness measurements from each participant's H^+ measurements are displayed in Table 2.2. The septum thickness measured in a horizontal direction across each of the Na^+ and H^+ gated and non-gated images did not differ by more than 3mm for each participant. The same was found when measuring the septum thickness with line profiles oriented at a 45-degree angle with respect to the image orientation. Figure 2.10 shows how the line profiles and septum widths changed as more cardiac data was included in the reconstruction of each image.

Table 2.1: Septum thickness means and ranges measured from each participant's Na⁺ MR images in two separate septum locations. Means include measurements from all gated and non-gated images. Max-min represents the largest difference in any two measured septum thicknesses.

	Horizontal		45-Degrees	
	Mean \pm Std (mm)	Max - Min (mm)	Mean \pm Std (mm)	Max - Min (mm)
Participant 1	7.9 \pm 0.4	1.1	9.3 \pm 0.6	1.5
Participant 2	7.9 \pm 0.1	0.4	8.3 \pm 0.1	0.2
Participant 3	7.8 \pm 1.1	2.6	5.1 \pm 0.6	1.5
Participant 4	9.6 \pm 0.5	1.4	10.4 \pm 0.3	0.7

Table 2.2: Septum thickness means and ranges measured from each participant's H⁺ MR images in two separate septum locations. Means include measurements from all gated and non-gated images. Max-min represents the largest difference in measured septum thicknesses.

	Horizontal		45-Degrees	
	Mean \pm Std (mm)	Max - Min (mm)	Mean \pm Std (mm)	Max - Min (mm)
Participant 1	9.5 \pm 0.0	0.0	9.5 \pm 0.3	0.5
Participant 2	10.0 \pm 0.2	0.4	8.2 \pm 0.5	1.0
Participant 3	6.5 \pm 0.4	0.7	6.1 \pm 0.1	0.2
Participant 4	8.5 \pm 0.3	0.5	9.8 \pm 0.1	0.2

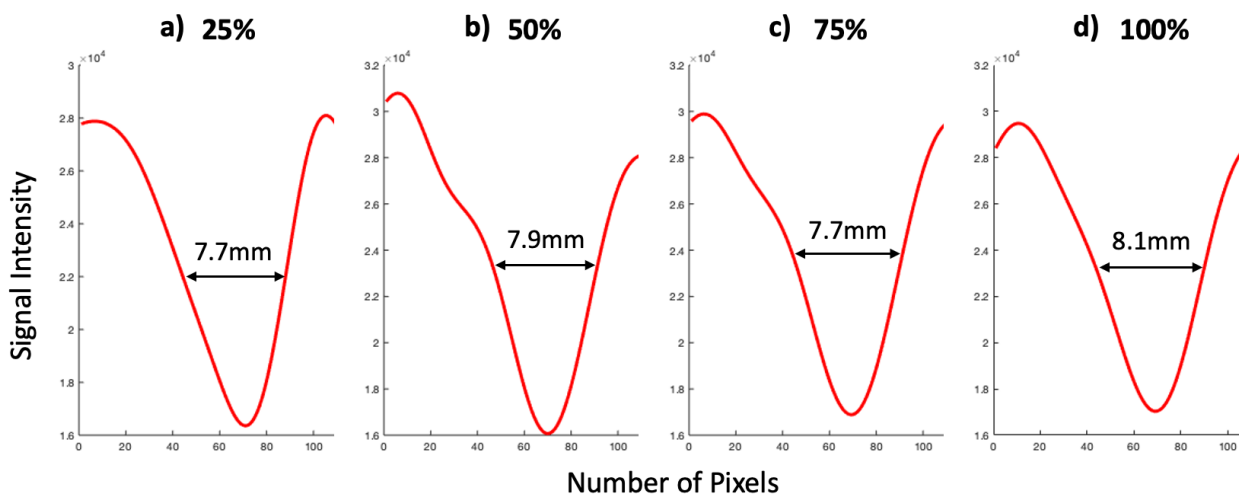


Figure 2.10: Line profiles and septum width measurements from sodium images of one participant containing data from a) 25%, b) 50%, c) 75%, and d) 100% of the cardiac cycle.

2.4 Discussion

Retrospectively gated cardiac Na^+ MR images acquired using a 3-T system do not exhibit significantly improved image quality when compared with non-gated images as determined by evaluation of PSFs, SNRs, and geometrical distortion.

For each participant, the FWHM of the PSFs of pixels from gated and non-gated Na^+ MR images were identical. Since the PSF is a measure of image resolution, it can be confirmed that the spatial resolution is conserved when retrospectively gating cardiac Na^+ MR images. However, the increase in signal fluctuations surrounding the peak of the PSF indicate that there is greater image blurring in the images that are gated. The prescribed in-plane resolution of our Na^+ imaging system is also higher (3mm) than similar studies investigating cardiac Na^+ ECG gating (5-6mm), but our slice thickness was made larger to maintain SNR.^{86,89,90}

For images that are further gated, the SNR was found to be significantly lower.

Specifically, the SNR of all tissue types in the Na^+ MR images increases according to the square root of the percent of cardiac cycle data included in the image. This was observed with R^2 values of each data set being very close to one, representing an almost-perfect fit.

This observation follows the expected relationship of SNR being proportional to the square root of the number of samples in an image. The images that are retrospectively gated have data omitted that were acquired when the heart was not at rest. These images therefore contain less samples than the images that are not gated. This causes SNR to decrease. Similar studies have also acknowledged that SNR decreases for cardiac sorted data.⁸⁶ To observe a similar SNR between gated and non-gated images, the number of samples must be the same in both images, and therefore the data acquisition must be at least 2-4 times longer. This is unrealistic in clinical settings, because the scan time for our Na⁺ imaging session is around 30 minutes and patients usually struggle to remain inside an MR scanner for any longer amount of time.

Regarding geometrical distortion, the maximum differences of cardiac septum measurements between gated and non-gated Na⁺ images did not exceed 3mm. This is the nominal resolution prescribed for this imaging experiment. A study investigating different correction methods for cardiac Na⁺ MRI acknowledges that the effects of cardiac motion on the resulting images are quite low compared to the spatial resolution of the imaging system.⁸⁶ The maximum differences of cardiac septum measurements between gated and non-gated H⁺ measurements also did not exceed their resolution (1.6mm). Therefore, there was no geometrical distortion detected in any of the images. This identifies that retrospectively gating Na⁺ as well as H⁺ MR images does not increase or decrease the apparent measurements of anatomical structures, specifically the septum.

Some limitations of this research study must be acknowledged. Na⁺ MRI is an imaging technique with low resolution (3 x 3 x 30 mm). These large image voxels can lead to partial volume errors in measurements, where voxels near the septum-ventricle barrier may contain sodium signal from both blood and cardiac muscle. The cardiac septum also changes in thickness throughout the cardiac cycle, although, the 3mm resolution is not fine enough to detect any change. During the data analysis, ECG peak detection was done manually since the magnet was not able to detect all heart beats. The Na⁺ images were also only corrected for cardiac motion, and not respiratory. However, the H⁺ images were acquired using breath-holds which lead to the same conclusions regarding geometrical

distortion. Additionally, the subjects imaged in our study did not cover all the possible cardiac differences, diseases, and rhythms that could potentially affect the results.

In conclusion, retrospectively gating cardiac Na⁺ MR does not improve image quality. Specifically, when comparing retrospectively gated images to non-gated images the spatial resolution and septum thickness measurements remained consistent, whereas the SNR of the gated images decreased. These results can be applied to additional studies using cardiac Na⁺ MRI, as extra scan time and technical adaptations can be avoided that are involved in the retrospectively gating process. Although studies have mentioned that cardiac gating must be used if quantifying the true myocardial Na⁺ signal from cardiac Na⁺ MR images, tissue sodium concentrations between gated and non-gated images do not differ by more than 5%.^{80,86} Another option may be to calculate ratios of cardiac Na⁺ signals from non-gated Na⁺ MR images, if comparing Na⁺ signals between participants without gating is desired.

Chapter 3

3 Intensity Correction for Cardiac Na⁺-MR Images Acquired with a Surface Coil

This chapter contains an analysis of two different signal intensity correction methods for Na⁺ MR images acquired with a surface coil with a condensed introduction (background, objectives, and hypotheses), as well as the main methodology, results, and discussion of this Master's thesis.

3.1 Introduction

3.1.1 Sodium (Na⁺) in the Body

Sodium (Na⁺) is the most abundant cation in the human body. It has an extracellular concentration that is 8-10 times higher than the intracellular, which is maintained by the sodium-potassium pump. The Na⁺ ion is essential for many processes in the human body, such as muscle contraction, nerve signal transmission, maintaining body water balance, and more. For this reason, proper Na⁺ balance is needed to maintain regular cell functioning, and disturbances in this balance can be indicative of disorders.^{43,54}

3.1.2 Sodium (Na⁺) MRI

Among all biological nuclei, Na⁺ provides the second strongest nuclear magnetic resonance signal in vivo, allowing it to be imaged with magnetic resonance imaging (MRI). Na⁺ MRI is beneficial, as it allows the non-invasive and direct analysis of tissue Na⁺ content, which is not possible by any other means. Therefore, imaging with Na⁺ MRI can provide information on tissue viability and states of disease. Previously, this method of imaging has been used to assess the tissue Na⁺ content of the brain in multiple diseases, breast and prostate cancer, the heart after myocardial infarction, the kidneys in patients with chronic kidney disease, and much more.⁴⁵

3.1.3 Sodium (Na^+) in Kidney Disease

Na^+ balance in patients with kidney disease is especially important because the kidneys are responsible for the majority of Na^+ excretion from the body. Na^+ MRI has shown promise for measuring dynamic sodium changes in healthy and diseased kidneys after water consumption.⁹⁴ Leg skin and muscle Na^+ in hemodialysis, chronic kidney disease, and heart failure patients has also been investigated to analyze trends in Na^+ content.^{75,95} An important finding of recent studies using Na^+ MRI, is that patients with kidney disease have Na^+ accumulation in their skin, bones, and muscle without excess water deposition.^{47,48,96} Their skin Na^+ content in particular has been found to be closely linked with cardiac abnormalities such as increased left ventricular mass.⁴⁰ Additionally, preclinical studies have demonstrated salt to promote fibrosis in the left ventricle of the heart.¹¹ Combining this information with the known increased cardiovascular risk in patients with kidney disease, it would be especially beneficial to analyze cardiac Na^+ content in kidney disease patients using Na^+ MRI.

3.1.4 Challenges of Sodium (Na^+) MRI

Na^+ MRI is difficult due to the inherent challenges presented by its nuclear properties and the limited concentration of sodium in most tissues. The Na^+ nucleus has a sensitivity for magnetic resonance which is about $1/11^{\text{th}}$ that of conventional proton MR imaging, and the Na^+ MR signal decays more quickly due to its quadrupolar moment.^{8,45} In addition to its limited endogenous concentration, this causes Na^+ MRI to have a very low signal-to-noise ratio (SNR). Furthermore, a radiofrequency (RF) coil tuned to specifically excite and detect Na^+ nuclei is required, which complicate the effort. These challenges combined with cardiac and respiratory motion cause cardiac Na^+ MR imaging to be especially difficult. At clinical MR field strengths of 3T, surface coils are often used for cardiac imaging.

3.1.5 Surface Coils

Surface coils are small (1-10cm diameter) RF coils that are used to image superficial structures in the body. Since single-loop surface coils are the simplest type of coils, they are commonly the first type of coil used for imaging nuclei other than protons.⁹⁷ In Na^+

imaging, surface coils are often operated in transmit-receive mode; they are used to excite the nuclei and detect the MR signal. Surface coils tend to have a higher signal-to-noise ratio than other coils due to their limited size and ability to receive signal only from nearby regions.⁹⁸ This offers a benefit to be used for cardiac Na⁺ MR imaging, offering high imaging sensitivity near their surfaces. However, sensitivity decreases rapidly with increasing distance from the centre of the coil. This limitation creates a problem during image analysis, as regions further away from the coil in the resulting image have a lower signal intensity. In scenarios where images are to be quantified for sodium concentration comparison between patients, this intensity drop-off must be corrected for.

3.1.6 Intensity Correction of Surface Coil Images

A paper by L. Axel et al describes two methods to correct for the intensity drop-off in surface coil MR imaging.⁸⁷ Using proton images of the wrist acquired with a 3cm wide rectangular surface coil, this study corrected for the intensity inhomogeneity by acquiring an additional image of a uniform phantom in the same position of the coil and divided the wrist image by the normalized phantom image. In this study, this method will be referred to as *phantom correction*. The second method they used involved dividing the original wrist image by a blurred version of itself to give an approximate correction. We will call this method *self-correction*. In our study, our objective was to analyze the accuracy these two methods for correcting the intensity of Na⁺ MR images of calibration vials obtained with an 18cm diameter surface coil, and then implement them in cardiac Na⁺ MR imaging for future clinical applications. Our hypothesis was that the phantom intensity correction method would be superior to the self-correction method, and that it would adequately correct for the intensity inhomogeneity in Na⁺ MR surface coil images.

3.2 Methodology

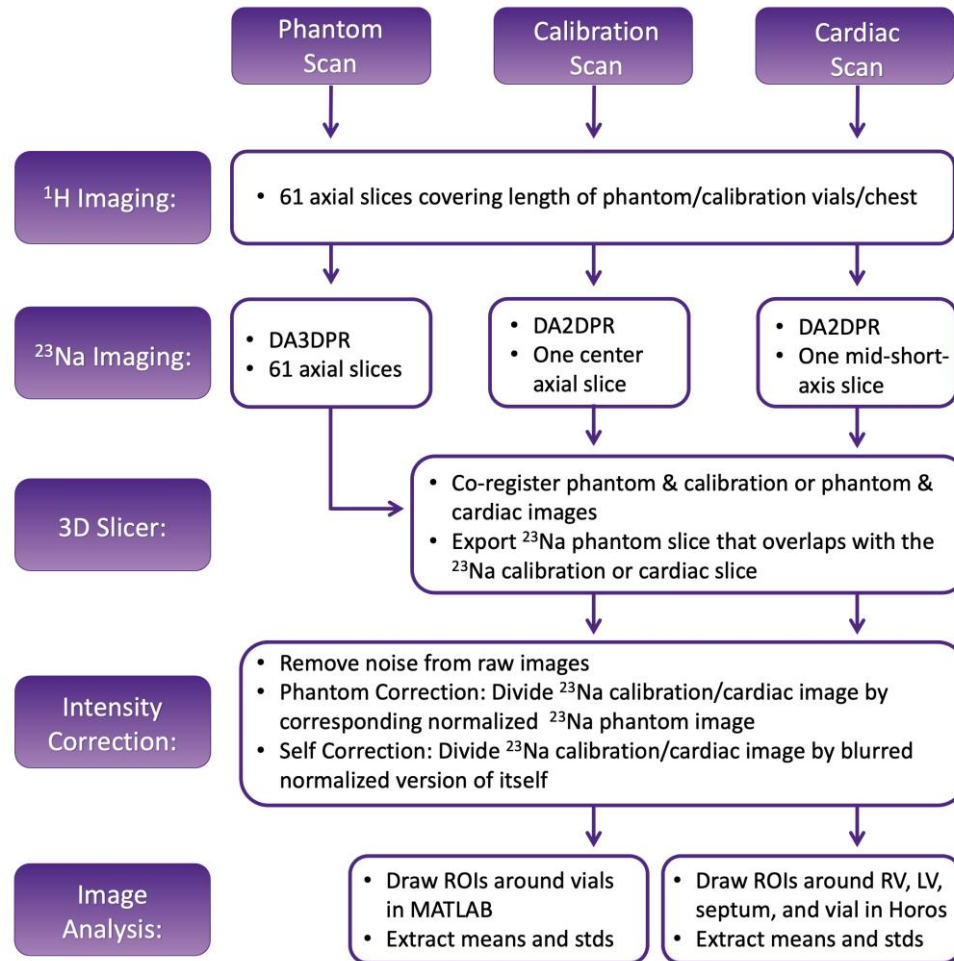


Figure 3.1: Flow chart displaying an overview of the project methods.

3.2.1 Study Design

This was a pilot cross-sectional cohort study where cardiac H^+ and Na^+ MRI scans of participants were acquired during a single study visit. Before any study visits took place, the study was approved by the University of Western Ontario Health Sciences Research Ethics Board. This study in whole was conducted in accordance with the approved protocol, Good Clinical Practice Guidelines, and all applicable regulatory requirements.

3.2.2 Participants

The study participants were recruited from London, Ontario, Canada. Participants with a previous history of cardiovascular disease or participants that did not pass the facility screening form were excluded from this study prior to written informed consent. Age of participants ranged from 23 to 37 years.

3.2.3 Sensitivity Correction Phantom MR Acquisition

All H^+ and Na^+ MR images in this study were acquired using a GE 3.0-T MRI system (Discovery MR750, General Electric Healthcare, Milwaukee, WI, USA). The phantom was a plastic container chosen to approximate the size of a human chest containing 150mM of NaCl dissolved in water.

All H^+ MR images in this study were acquired using the built-in body coil in the MR scanner. Axial images covering the entire length of the phantom in 61 slices were acquired using a 2D fast imaging employing steady state acquisition (FIESTA) non-gated pulse sequence with the following parameters: flip angle = 50° , FOV = $36 \times 36\text{cm}^2$, in-plane resolution = $3 \times 3 \text{mm}^2$, slice thickness = 3mm, repetition time = 3ms, and no spacing.

All Na^+ MR images in this study were acquired using a custom built single-loop (18cm diameter) radiofrequency (RF) surface coil tuned for the Na^+ nucleus (33.786 MHz). The RF coil was placed on the top centre of the phantom, and a 100mM NaCl calibration vial was positioned diagonally above the coil. There were also 6 vitamin pills placed within the plane of the RF coil to act as fiducial markers during image processing, which were visible in both H^+ and Na^+ images. The experimental setup is shown in Figure 3.2. The pulse sequence used for Na^+ imaging was a density adapted 3D projection reconstruction (DA3DPR) pulse sequence with the following parameters: isotropic FOV = $36 \times 36\text{cm}^2$, resolution = $3 \times 3 \times 3 \text{mm}^3$, TR = 100ms, TE = 0.5ms, flip angle = 90° , signal averages = 1, radial projections = 11310, acquisition time = 18.5 minutes. Axial Na^+ MR images were acquired in 61 slices with a slice thickness of 3mm, in-plane resolution of $3 \times 3 \text{mm}^2$, and no spacing. The imaging sequence was repeated three times to increase SNR.

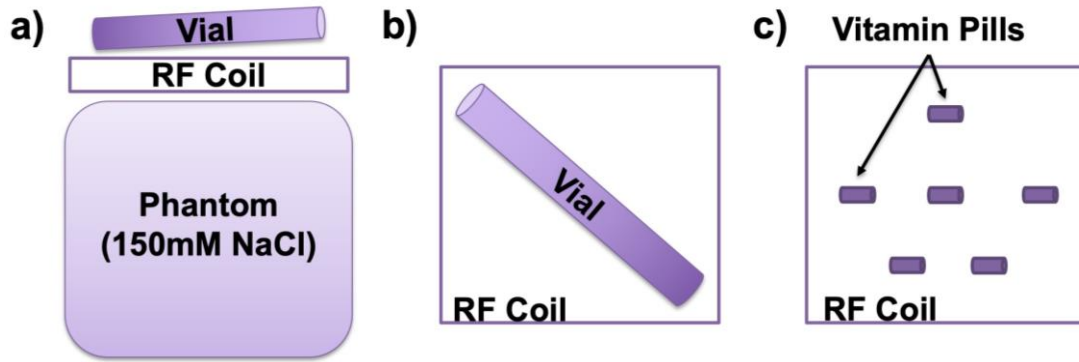


Figure 3.2: Phantom experimental setup in the a) axial plane and in the b) coronal plane showing the location of the vial and c) vitamin pills within the coil. The phantom contained 150mM of NaCl and the external calibration vial contained 100mM of NaCl.

3.2.4 Calibration Vials MR Acquisition

H^+ and Na^+ MR images of a cluster of nine calibration vials were imaged, each with a concentration of either 50mM, 100mM, or 150mM of NaCl. The arrangement of these vials with respect to the RF coil is shown in Figure 3.3. The cluster of calibration vials were submerged in a large plastic bin filled with 50mM of NaCl before scanning.

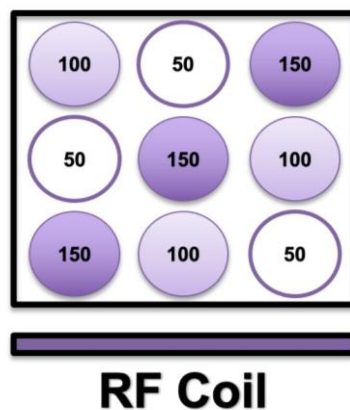


Figure 3.3: Visual representation of the arrangement of vials with respect to the RF coil. Values represent the concentration of NaCl in each vial in millimoles per liter.

For the H⁺ images, 61 axial images were acquired to cover the entire length of the calibration vials with the same 2D FIESTA non-gated pulse sequence as the phantom H⁺ images (in-plane resolution 3 x 3mm², slice thickness of 3mm, no spacing).

For the Na⁺ images, the RF coil was placed beneath the plastic bin, in the centre of the cluster of calibration vials. The same external 100mM calibration vial was placed diagonally beneath the RF coil, and the 6 vitamin pills remained inside the casing of the RF coil to act as fiducial markers. A density adapted 2D projection reconstruction (DA2DPR) pulse sequence was used to acquire one centre axial Na⁺ image slice of the calibration vials with the following parameters: FOV = 36 x 36cm², in-plane resolution = 3 x 3 mm², TR = 100ms, TE = 1.2ms, flip angle = 90°, signal averages = 50, radial projections = 378, acquisition time = 31.5 minutes, and a slice thickness of 30mm.

These H⁺ and Na⁺ calibration scans were repeated three times on three separate days as a measure of reproducibility.

3.2.5 Cardiac MR Acquisition

Cardiac H⁺ and Na⁺ MR images were acquired of each participant. Participants were placed in the MR scanner in feet-first supine position with electrocardiogram leads placed on their chest for cardiac gating purposes.

For the H⁺ images, 61 axial images were acquired to cover the entire length of the heart with the same 2D FIESTA non-gated pulse sequence as mentioned previously (in-plane resolution 3 x 3 mm², slice thickness of 3mm, no spacing). One H⁺ mid-short-axis slice was also acquired of each participant's heart to guide the drawing of regions of interest (ROIs) during image analysis. These images were mid-short-axis images prospectively gated and acquired during repeated breath-holds with a 2D CINE FIESTA pulse sequence with the following parameters: TR = 3.5ms, TE = 1.5ms, flip angle = 45°, FOV = 36 x 36cm², matrix = 512 x 512, slice thickness = 30mm, and 25 cardiac phases.

For the Na⁺ images, the RF coil was placed on the participant's chest above their heart and the same 100mM calibration vial was positioned diagonally above the coil. The 6 vitamin pills remained in the casing of the RF coil to act as fiducial markers. The position of the coil was adjusted, if needed, to have the centre of the coil directly above the centre of the participant's left ventricle. This was determined using H⁺ localizers obtained by the built-in MR body coil. Before Na⁺ imaging, a shift reagent was used to ensure a 90° flip angle. The same DA2DPR pulse sequence was used to acquire the cardiac Na⁺ MR images. One cardiac Na⁺ mid-short-axis MR image slice was acquired of each participant's heart with an in-plane resolution of 3 x 3mm² and a slice thickness of 30mm.

3.2.6 Image Processing

The Na⁺ MR raw k-space data was used to reconstruct the axial Na⁺ images for the phantom and calibration vials with a 256x256 matrix in MATLAB (Mathworks, R2020a, Natick, MA) using a non-uniform fast Fourier transform toolbox and re-gridding algorithm.⁹⁹

For each of the three calibration scans, the axial H⁺ phantom and axial H⁺ calibration images were co-registered using 3D Slicer software (<http://www.slicer.org>).¹⁰⁰ Images were co-registered manually by applying a linear transformation to the axial H⁺ calibration images. This was done by aligning the fiducial markers in both images sets that were visible within the imaging region of the RF coil. These same transformations were then applied to the Na⁺ calibration image to ensure the Na⁺ calibration image was co-registered with the Na⁺ phantom images. Using the linear interpolation resampling module in 3D Slicer,¹⁰⁰ one phantom Na⁺ slice was exported that contained all of the phantom Na⁺ pixels that overlapped the Na⁺ calibration image slice. The intensity of each pixel in the exported 3 x 3 x 30mm Na⁺ phantom slice was an average of the intensity of all overlapping pixels in that region from the original Na⁺ phantom image set. This new Na⁺ phantom image was a single slice that lay in the same region under the RF coil as the Na⁺ calibration image that was needed for intensity correction.

Before intensity correction, the mean signal offset that was created from noise was subtracted from the Na⁺ calibration magnitude image. This was done in MATLAB (Mathworks, R2020a, Natick, MA) by using the following equation that was described in a paper by A. Miller and P. Joseph:¹⁰¹

$$M_c^2 = M^2 - M_0^2 \quad [3.1]$$

In this equation, M is the raw image, M_0 is the image background noise, and M_c is the image with the noise removed.

The intensity corrections were made using custom scripts written in MATLAB (Mathworks, R2020a, Natick, MA) according to methods described by L. Axel et al.⁸⁷ For the phantom correction, the Na⁺ phantom image extracted from 3D Slicer¹⁰⁰ was first normalized so all pixel intensity values were between 0-1. The Na⁺ calibration image with noise removed was then divided by the normalized Na⁺ phantom image to produce the phantom intensity corrected Na⁺ calibration image. For the self-correction, the Na⁺ calibration image was blurred and normalized, and the original image was divided by the blurred version to produce the self-corrected Na⁺ calibration image. For images produced by both methods, an ROI was drawn around the 100mM NaCl vial located above the RF coil in the image, the mean was calculated, and the image was normalized using this value. The image was then multiplied by 100 to scale the pixel intensity values to reflect the actual Na⁺ concentration in the image.

Each of these steps (image reconstruction, co-registration, phantom Na⁺ image export, noise removal, intensity correction, and image rescaling) were repeated for each participant's mid-short-axis cardiac Na⁺ image, just as they were for the calibration images. The original calibration and cardiac Na⁺ images also underwent noise removal and rescaling to serve as a comparison during image analysis. All final images were exported to DICOM files.

3.2.7 Image Analysis

The original and intensity corrected Na⁺ calibration images were analyzed using MATLAB. The MATLAB code drew circular ROIs with identical diameters around each vial and extracted mean Na⁺ signals and standard deviations.

All original and intensity corrected cardiac Na⁺ DICOM files were uploaded into the medical image software viewer Horos (Version 3.3.6). In Horos, ROIs were drawn around the external vial, left ventricle (LV), right ventricle (RV), and septum of the heart in the original image using the mid-short-axis cardiac H⁺ images as a guide. These ROIs were copy and pasted onto the phantom and self-corrected cardiac Na⁺ images of the corresponding participants. Mean Na⁺ signal intensities were extracted from these ROIs as well as their standard deviations.

3.2.8 Statistical Analysis

Interobserver variability was calculated between two independent readers (T.M and J.T). The intraclass correlation coefficient was calculated for the signals of each vial (50mM, 100mM, and 150mM) between the three calibration scans and also between readers using the two-way mixed model for average measures. The intraclass correlation coefficient was calculated for the signals of each ROI (right ventricle, left ventricle, septum, and external vial) in the cardiac Na⁺ images using the two-way mixed model for single measures. Statistical analyses were performed with IBM SPSS software (IBM Corp. Released 2021. IBM SPSS Statistics for Windows, Version 28.0. Armonk, NY: IBM Corp).

3.3 Results

3.3.1 Calibration Scans

The vials from the original, self-corrected, and phantom corrected calibration images of one of the three calibration scans are shown in Figure 3.4. Visually, the vials that contain the same concentrations of NaCl have a similar signal intensity after self-correction and phantom correction.

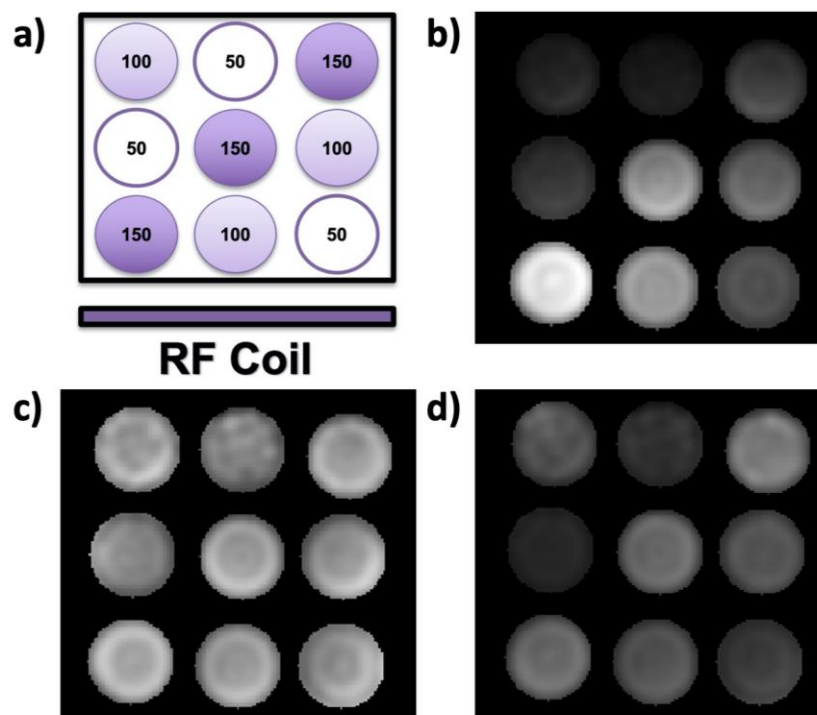


Figure 3.4: a) Arrangement of coil and vials with concentrations. b) The original, c) self-corrected, and d) phantom corrected Na^+ MR calibration images of one of the three calibration scans.

Figure 3.5 displays a graph of mean signal intensities versus known Na^+ concentration for one of the three calibration scans. The values are separated by correction method, and each data point is the mean of the three signal intensities of the vials of the same concentration in the image. The slope of the line of best fit connecting these data points is 0.85 with 95% confidence interval [0.17, 1.5] for the phantom corrected and 0.26 with 95% confidence interval [-0.52, 1.0] for the self-corrected. The standard deviations of the mean signal intensities were substantially lower in the phantom corrected and self-corrected images compared to the original. The two remaining calibration scans provided similar results, with their mean signal intensities shown in Table 3.1.

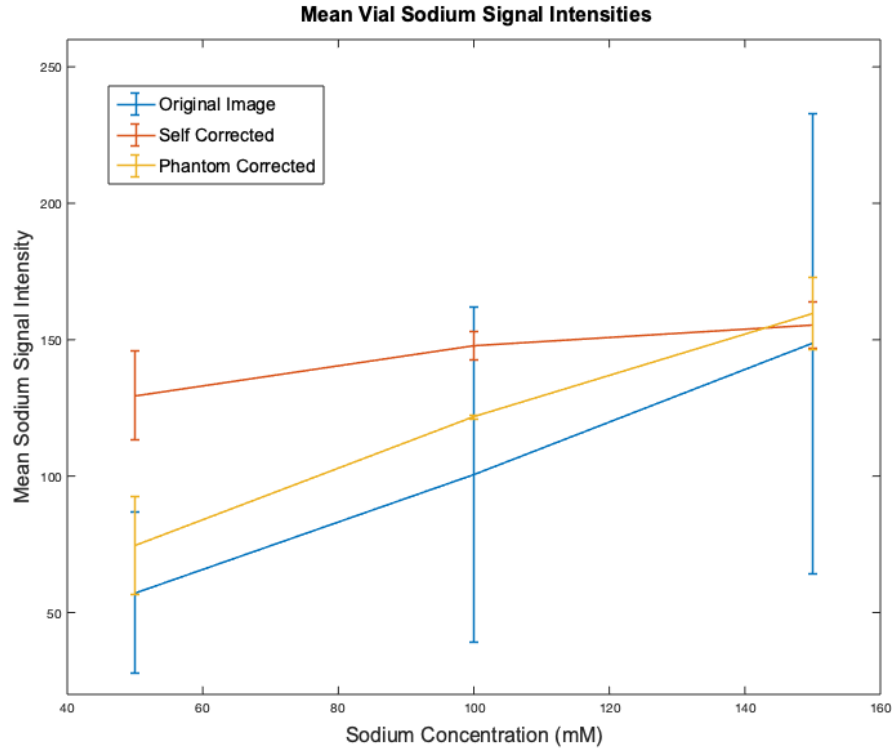


Figure 3.5: Mean vial sodium signal intensities versus known sodium concentration.
Each data point represents the mean of three vial signal intensity measurements.
Error bars represent the standard deviation values for each data point.

Table 3.1: Mean Sodium Signal Intensities of Calibration Vials for Three Repeated Scans

	Original (mean ± std)			Self-Correction (mean ± std)			Phantom Correction (mean ± std)		
	#1	#2	#3	#1	#2	#3	#1	#2	#3
50mM	56.9 ± 25.1	59.3 ± 31.6	57.1 ± 29.6	128.8 ± 12.9	129.0 ± 13.7	129.6 ± 13.3	67.4 ± 7.2	77.9 ± 20.5	74.6 ± 17.9
100mM	97.6 ± 54.4	102.9 ± 64.9	100.5 ± 61.4	148.3 ± 4.8	148.7 ± 4.4	147.7 ± 4.2	122.1 ± 7.3	123.1 ± 3.4	121.7 ± 0.7
150mM	145.7 ± 88.1	155.8 ± 100.0	148.5 ± 84.4	154.8 ± 6.2	155.9 ± 7.2	155.3 ± 6.9	158.0 ± 15.5	158.8 ± 7.8	159.6 ± 13.2

3.3.2 Cardiac Scans

Figure 3.6 shows a proton and uncorrected sodium mid-short-axis slice of one participant's heart that was used for analysis. Superimposing the images allows visualization of the Na^+ signal with respect to cardiac anatomy.

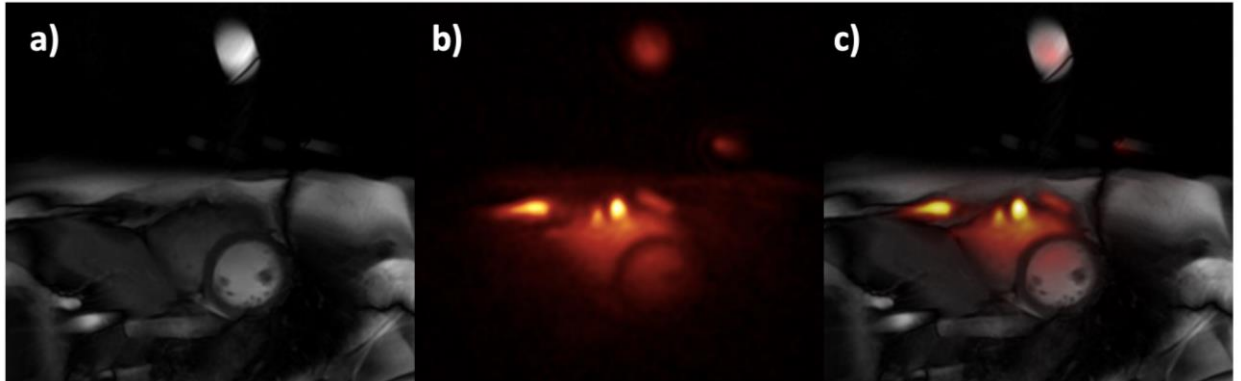


Figure 3.6: Mid-short-axis slice acquired by a) proton and b) sodium MRI. Proton and sodium images are superimposed in image c). Increased intensity in the sodium image represents higher sodium concentration in that region.

Original, self-corrected, and phantom corrected cardiac Na^+ MR images of one participant are shown in Figure 3.7. Visually, the region of the image that is more distant from the coil (lower half) shows a boost in signal after correction by both methods.

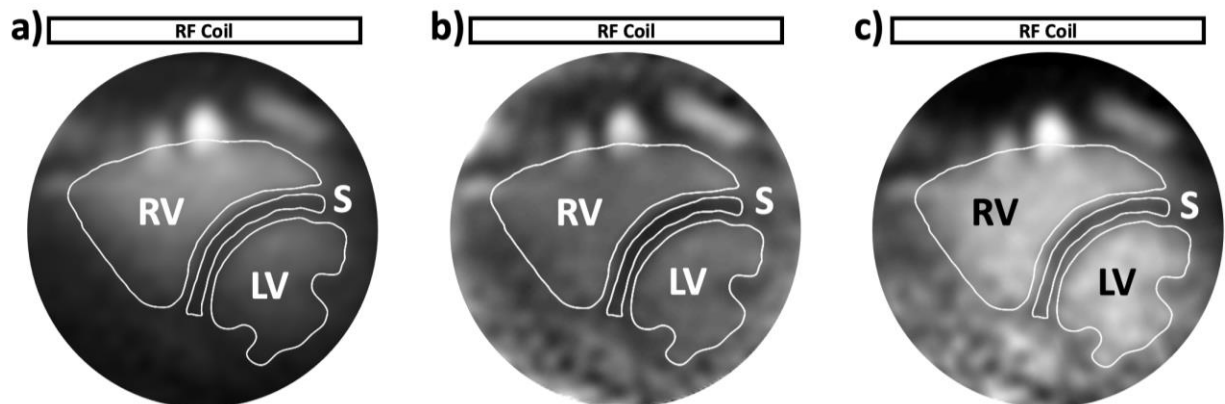


Figure 3.7: The a) original cardiac Na^+ MR image of one participant, and the image after b) self-correction, and c) phantom correction with regions of interest (ROIs)

displayed. The ROIs are labelled to show the right ventricle (RV), left ventricle (LV), and septum (S). Coil location shown.

Figure 3.8 displays the mean Na^+ signal ratios for the original cardiac Na^+ images, whereas figure 3.9 shows the ratios for the phantom corrected images. In comparison to the original image values, the phantom corrected images provide much more consistent ratios and lower uncertainties when using the signal in the ventricles as a reference. The ratio of Na^+ signal in the septum over the external vial did not give consistent results. Table 3.2 shows groups averages of the sodium signal ratios measured from the phantom corrected images.

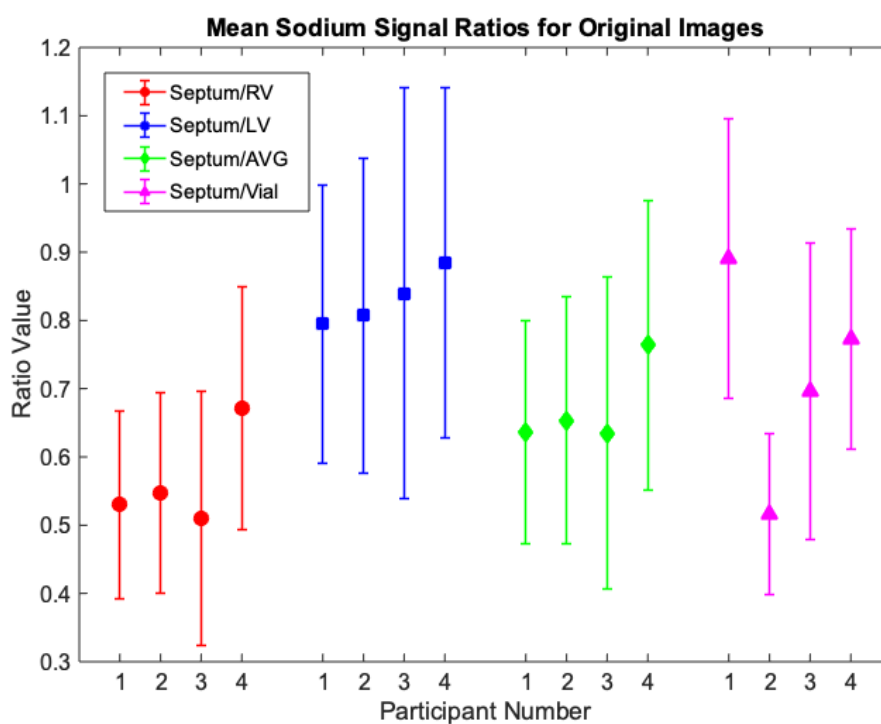


Figure 3.8: Mean sodium signal ratios for the original cardiac sodium images. Ratios are separated by participant number and ratio type. Ratios include the mean signal in the septum over the mean signal in the right ventricle (RV), left ventricle (LV), average signal in both ventricles (AVG), and external 100mM NaCl vial. Error bars represent the uncertainty in each ratio, calculated from the standard deviations of the signal intensities in each ROI.

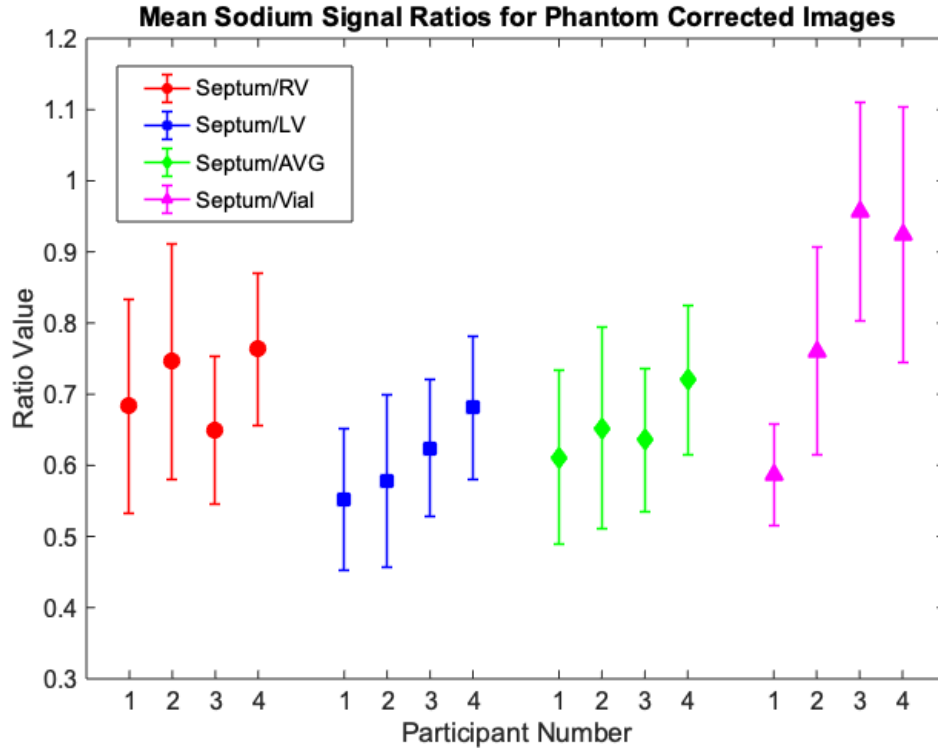


Figure 3.9: Mean sodium signal ratios for the phantom corrected cardiac sodium images. Ratios are separated by participant number and ratio type. Ratios include the mean signal in the septum over the mean signal in the right ventricle (RV), left ventricle (LV), average signal in both ventricles (AVG), and external 100mM NaCl vial. Error bars represent the uncertainty in each ratio, calculated from the standard deviations of the signal intensities in each ROI.

Table 3.2: Group Averages of Sodium Signal Ratios for Phantom Corrected Images

	Septum/RV	Septum/LV	Septum/AVG	Septum/Vial
Group Averages (mean ± std)	0.71 ± 0.05	0.61 ± 0.05	0.65 ± 0.04	0.70 ± 0.25

3.3.3 Interobserver and Interscan Variability

The intraclass correlation coefficient measures for interobserver variability were 0.97 for the calibration vial scans and 0.99 for the cardiac ROIs. The intraclass correlation coefficient for interscan variability between the three separate calibration vial scans was 0.99.

3.4 Discussion

Cardiac Na⁺ MRI holds potential to measure and compare cardiac tissue Na⁺ signals between healthy and diseased participants to provide clinical insight. Surface coils are commonly used for this type of image acquisition at 3-T because of their simplicity, increased local SNR, and ability to be positioned proximal to the anatomical region being imaged. Their significant limitation is that signal intensity produced by these coils decreases rapidly with depth into the participant, which often limits their application for imaging deeper structures within the body. Correcting for this surface coil limitation has been shown to increase successful diagnosis and decrease time of image interpretation as mentioned in a study by Ren et al. studying spinal metastases with proton MRI.¹⁰² In this work we set out to correct for the signal intensity drop-off in Na⁺ images acquired with a surface coil using two separate methods, evaluate their reliability, and apply them to human cardiac images. As the results of this study show, the phantom intensity correction method is an accurate means of ameliorating the sensitivity profile of the Na⁺ surface coil providing more image uniformity for sodium image analysis.

Although both the phantom correction and self-correction method appear to improve signal intensity homogeneity, the self-correction method significantly decreases the contrast in the resulting images. In the calibration scan analysis of the self-correction method, all vials appear to contain similar signal intensities based on their brightness, despite the change in vial NaCl concentration. The low slope of the self-corrected data when measured Na⁺ signal is plotted against known Na⁺ concentration of the calibration vials also displays this reduction in contrast. This is occurring because dividing an image by its blurred version causes signal intensity values to converge, which also depends on the degree to which blurring is performed. The blurring method used in this study was 2D gaussian filtering, which was good for visualization but not quantification. The self-correction method therefore would not be an appropriate method to apply to images before extracting and comparing image values between participants. This method would not properly assess the underlying Na⁺ concentrations in tissue and would not be able to characterise disease states.

The phantom intensity correction method increases signal intensity homogeneity while retaining image contrast. With this correction method, measured Na^+ signal intensities correlate with the known Na^+ concentration in the calibration vials. This is shown by the slope nearly equal to one in the mean vial Na^+ signal intensity graph for this correction method. The low standard deviations of this data set also show that vials of the same Na^+ concentration consistently provide similar Na^+ signal intensities. Although these two observations are expected results of an ideal correction method, this method does not have the ability to improve the SNR in areas distant from the surface coil. Other studies using this correction method have also mentioned this limitation,^{87,103} which becomes particularly applicable when using imaging modalities with low inherent SNR such as Na^+ MRI. This limitation impacts this study because measurements in regions more distant from the coil will have higher noise, therefore measurements will have larger standard deviation values and will be less precise.

When applied to human cardiac Na^+ MR images, the phantom intensity correction method once again visually improved signal intensity homogeneity. The ratio of mean Na^+ signal in the cardiac septum over the mean Na^+ signal measured from the blood pools in the ventricles provides a consistent value to represent the cardiac Na^+ signal in a participant. Our group average value of myocardial to blood Na^+ signal after correction (0.65) is very similar to the same ratios interpreted from the results of other research papers (0.66-0.68) that investigated cardiac Na^+ signals of healthy participants using various acquisition methods with field strengths other than 3T.^{90,104,105} The blood in the ventricles provides an internal standard to compare with the myocardial signal if the Na^+ in the blood has low inter and intrasubject variability. However, controls and patients with CKD are likely to have high variability of serum sodium levels. Internal standards have been successfully used in Na^+ imaging previously, with the Na^+ signal of cerebrospinal fluid used to estimate the Na^+ concentration in the intervertebral disk.¹⁰³ Ventricular blood as an internal standard could be used in future studies to compare cardiac tissue Na^+ signals between healthy and diseased participants if serum sodium was collected. However, one limitation with using the signal of blood in the ventricles

includes the blood signal varying depending on the direction and velocity of blood flow during imaging.

The external Na^+ calibration vial in the cardiac scans was not found to be a reliable standard for measurement, as it led to inconsistent Na^+ ratios. A study by Christa et al. studying cardiac Na^+ signals in patients with primary hyperaldosteronism and controls found the Na^+ signal ratio of interventricular septum to an external 100mM NaCl vial in controls to be 0.21. Sensitivity correction was incorporated in this study, but their ratio substantially differs from our observed results. It is not possible to determine the reason for the differences without details on their intensity correction methods. Other studies have reported explicit measurements of Na^+ signal concentrations. Lott et al. reported a myocardial tissue Na^+ concentration of (54 ± 5) mM before correction,¹⁰⁴ and Ouwerkerk et al. reported (53 ± 12) in the septum.¹⁰⁵ Based on these studies, a Na^+ signal ratio of the septum to an external 100mM NaCl should give a value closer to 0.54. During our image analysis, it was noticed that our external vial was not producing a uniform signal intensity to be used as a reference, as its measurement was giving a high standard deviation. This could be attributed to the change in the orientation of the 30mm thick image slice between participants, always perpendicular to the cardiac long axis, which was not always perpendicular to the vial. To solve this problem, a uniform sheet phantom was tested but was found to affect patient comfortability in the scanner. Since the external vial was used to rescale the images, cardiac Na^+ values are displayed as ratios and not true concentrations. The Lott et al. group was able to report explicit cardiac concentrations because they were using a 7T scanner with a birdcage coil.¹⁰⁴ With 3T scanners such as the scanner used in our study, a surface coil must be used to acquire optimal SNR in the resulting images, and therefore requires intensity correction. The Ouwerkerk et al. group quantified cardiac Na^+ using adiabatic pulses and reference vials, but with axial images of the heart.¹⁰⁵ We acquired mid-short-axis images in our study to minimize partial volume effects in the heart, which limited our ability to report absolute Na^+ concentrations using the reference vial.

In conclusion, the phantom intensity correction method is adequate to correct for the intensity drop-off in surface coil Na^+ MR images and has been proven to be reproducible. This method shows promise to be able to identify whether the cardiac septum is a novel site of Na^+ storage, and whether cardiac Na^+ tissue content may be involved in negative cardiovascular outcomes in kidney disease patients.

Chapter 4

4 Conclusions and Future Work

This chapter contains a summary of the overall findings in this thesis, limitations of the research, and expected future work.

4.1 Discussions and Conclusions

Chronic kidney disease (CKD) is known to be a major risk factor for cardiovascular disease, however, the direct link between these conditions remains unclear. Patients with CKD have damaged kidneys that can lead to inadequate removal and accumulation of sodium. In CKD patients on hemodialysis therapy, this has been found to occur in the skin, bones, and muscle.⁴⁹ Specifically, in preclinical studies sodium accumulation in the myocardial tissue has been found to induce fibrosis formation and other factors that contribute to heart failure.^{11,77} This study was created with the intent of quantifying myocardial tissue sodium in healthy and diseased kidney patients with cardiac Na⁺ MRI to determine whether increased myocardial sodium correlates with myocardial fibrosis and cardiac abnormalities. However, before myocardial tissue sodium could be properly measured and compared between individuals, the imaging pipeline had to be optimized. Therefore, this thesis focused on technical adaptations of cardiac Na⁺ MRI, including cardiac electrocardiogram (ECG) gating and signal intensity correction. This study investigated whether implementing ECG gating would increase image quality, and whether the signal intensity inhomogeneity from surface coil imaging could be adequately corrected.

In chapter 2 of this thesis, we investigated whether implementing ECG gating would improve our cardiac Na⁺ MR image quality. Image quality was assessed using image SNR, point spread functions for resolution, and geometrical distortion. Contrary to our hypothesis, our images acquired with retrospective ECG gating did not have improved image quality. Gated images had a decreased SNR, whereas spatial resolution and geometrical distortion measured by point spread functions and septum thicknesses remained unchanged. It was found that future studies using Na⁺ MRI at in-plane

resolutions of $3 \times 3 \text{ mm}^2$ can avoid the extra havoc of implementing gating – if all imaging parameters are kept equal, gating reduces SNR due to data omitted during cardiac contraction.

In chapter 3 of this thesis, we determined an imaging pipeline to adequately correct the signal intensity inhomogeneity in our Na^+ MR images caused by surface coil imaging. This pipeline included removing the noise from the raw images, imaging a phantom with uniform saline concentration, and dividing the cardiac Na^+ images by the phantom Na^+ images. It was first assessed using a sodium calibration vial scan, where it was found to increase signal intensity homogeneity, providing signal intensities that are proportional to the known sodium concentrations in the vials. The pipeline was then used on cardiac images to assess whether it could be used for future imaging studies that measure and compare myocardial sodium signals. It was found that after intensity correction, the ratio of mean Na^+ signal in the cardiac septum over the mean Na^+ signal of ventricular blood provides a consistent value to represent myocardial sodium signal. In the future, studies comparing myocardial sodium between individuals can use the blood in the ventricles as an internal reference standard if serum sodium is collected.

This study contributes to existing literature as it provides additional information on imaging techniques and post-processing needed for cardiac Na^+ MR image analysis. Similar studies have investigated the effects of ECG gating on cardiac Na^+ MR imaging, although, these studies were using scanners with higher field strengths and lower resolution.^{86,89,90} Our study used an in-plane resolution of $3 \times 3 \text{ mm}^2$ and a 3-T scanner, which are easier accessible and clinically applicable. Previous studies have also implemented intensity correction techniques, using additional images of a uniform phantom to correct signal non-uniformity created by surface coil imaging.^{87,103} Our study is the first to successfully apply these methods to cardiac Na^+ MR images. Na^+ MRI is an evolving field of research, specifically in terms of tissue sodium quantification in disease states. In healthy controls, previous literature using various methods have mentioned septum to ventricle blood sodium ratios that are highly comparable to our findings.^{85,86,90} The results of this study will therefore allow myocardial tissue sodium content to be

assessed and compared between healthy individuals and those with cardiac complications – such as patients with kidney disease.

4.2 Challenges and Limitations

4.2.1 COVID-19 Pandemic

The COVID-19 pandemic has substantially impacted graduate student research and experience over the past two years. For my intended project, the pandemic delayed research ethics board approval and affected the recruitment of participants. Participants were more hesitant to volunteer for a scan due to the risks of spreading COVID-19. The extra safety protocols in place also added extra barriers to participation. Access to the scanner was denied during the lockdowns, and scan time was hard to come by when research centers reopened. The majority of the work for my thesis was completed remotely, with less access to mentorship and resources. Regardless, I was able to complete a meaningful study with results that will influence future work in our laboratory.

4.2.2 Limitations of Na⁺ MRI

Na⁺ MRI is a valuable imaging tool, however, it has many limitations when compared to conventional H⁺ MRI. Sodium has a much lower concentration in the body, giving rise to Na⁺ MRI's lower sensitivity which is about 1/11th of H⁺ MRI. Its lower sensitivity is also due to sodium's lower gyromagnetic ratio (11.262 vs. 42.577 MHz/T). The sodium nucleus also has a spin value of 3/2 creating a quadrupolar moment. The quadrupolar moment causes the sodium MR signal to decay much faster than the proton with short T1 and rapid bi-exponential T2 relaxation. Each of these factors contribute to the lower SNR in Na⁺ MR images. To overcome these challenges, imaging is done at lower resolutions and image sequences are often much longer to collect more signal data. In our study, our in-plane resolution was 3 x 3 mm², our slice thickness was 30mm, and our acquisition was 31.5 minutes to collect enough data to achieve an adequate SNR for analysis. Additionally, the MR scanner must be equipped with transmit and receive RF coils that are tuned to the specific resonant frequency of the sodium nucleus. This imaging hardware for Na⁺ MRI is not widely available and can be costly to manufacture. For our

study, our RF coils were custom-built for our needs, which took a lot of tuning and modifications. Even with these adaptations, Na⁺ MRI has limited ability to recover anatomical structures, provide detailed accurate information, and would have challenges being applied in a clinical setting.

4.2.3 Sodium Quantification

One of the goals of our work was originally to quantify myocardial tissue sodium. Quantification was eventually not found to be feasible with the imaging protocol and pipeline used. Hence, sodium signal ratios were used in chapter 3. For quantification to be possible, the signal intensity in Na⁺ MR images must be uniform, proportional to the sodium concentration in vivo, and a reference of known sodium concentration in the image is needed. In our cardiac Na⁺ MR images, our reference vial did not produce a uniform signal intensity needed for quantification. Regardless, sodium signal ratios were still able to provide us with a relative sodium signal in comparison to an internal standard that can be compared between individuals or patient groups in future studies.

Alternatively, sodium could potentially be quantified from the images by using the blood as an internal reference if a basic metabolic panel of the participant is done to determine blood sodium concentration during the study visit. However, the sodium signal from ventricular blood in the resulting MR image can vary depending on the velocity and direction of blood flow.

4.2.4 Application to Future Work

Cardiac Na⁺ MRI is a field of study warranting further investigation, however, future studies may have challenges applying our results to patient groups. Since MRI is a quite expensive imaging modality, population sizes in this study were kept small. The goal was to find preliminary results to apply to a larger patient study in the future. Considering the small number of participants, we did not image all possible cardiac variations. We only imaged healthy participants, so it's likely other challenges will be encountered when applying these imaging methods to diseased individuals. Specifically, those with cardiac arrhythmias, LVH, or other cardiac abnormalities. Our imaging protocol is also quite long, with our acquisition time totaling to about 1.5 hours after Na⁺ and H⁺ MRI. This protocol

also included additional sequences being investigated for application to the future patient study. From experience, some patients have difficulties remaining inside the scanner for longer than 30 minutes. This is another reason why it may be difficult to apply our imaging protocol to future patient studies. Additionally, the results of this study are only attributable to current sodium imaging systems using an in-plane resolution of $3 \times 3 \text{ mm}^2$ and a slice thickness of 30mm. If resolution were to increase, our results may no longer be applicable. Due to all these limitations, the specialized equipment needed for sodium imaging, and the post-processing required, Na^+ MRI is far from being implemented in clinical settings for diagnosis and treatment purposes.

4.3 Future Work

As mentioned, this study was conducted preliminary to an intended study that will analyze myocardial sodium content of kidney disease patients and controls. The goal of this future work is to determine whether sodium content in the septum correlates with biomarkers for cardiac fibrosis and cardiac abnormalities in patients with compromised kidneys. This study is currently underway as it's using the results of the technical adaptations tested in this thesis for sodium imaging. Specifically, this study is using the phantom intensity correction method and sodium septum ratios presented in this thesis to be able to compare septal sodium content between individuals.

This study will be imaging hemodialysis patients, patients with chronic kidney disease, and healthy controls using Na^+ and H^+ MRI. Na^+ MRI will be used to assess sodium content in the septum, and H^+ MRI will be used to assess cardiac function. Measures of cardiac function will include EDV, ESV, LVM, and LVEF. T1 and T2 mapping will also be implemented that are known to assess cardiac fibrosis and edema. After imaging, sodium signal ratios, cardiac function parameters, and fibrosis levels will be compared between sex and age matched hemodialysis patients, chronic kidney disease patients, and healthy controls.

Chronic kidney disease is known to be a major risk factor for cardiovascular disease, however, the direct relationship between these diseases remains unclear. It is postulated that if myocardial sodium content is found to correlate with fibrosis and decreased

cardiac function, it may be involved in the cardiovascular disease-chronic kidney disease comorbidity. These results are important as they have the potential to identify a novel site of sodium storage. Furthermore, they could lead to additional studies investigating therapeutics that target the myocardium, mobilize the accumulated sodium, and potentially improve cardiovascular outcomes in chronic kidney disease patients.

References

1. Bikbov B, Purcell CA, Levey AS, et al. Global, regional, and national burden of chronic kidney disease, 1990–2017: a systematic analysis for the Global Burden of Disease Study 2017. *Lancet*. 2020;395(10225):709-733. doi:10.1016/S0140-6736(20)30045-3
2. Di Lullo L, Gorini A, Russo D, Santoboni A, Ronco C. Left Ventricular Hypertrophy in Chronic Kidney Disease Patients: From Pathophysiology to Treatment. *CardioRenal Med*. 2015;5(4):254-266. doi:10.1159/000435838
3. Edwards NC, Moody WE, Chue CD, Ferro CJ, Townend JN, Steeds RP. Defining the natural history of uremic cardiomyopathy in chronic kidney disease: The role of cardiovascular magnetic resonance. *JACC Cardiovasc Imaging*. 2014;7(7):703-714. doi:10.1016/j.jcmg.2013.09.025
4. Rutherford E, Talle MA, Mangion K, et al. Defining myocardial tissue abnormalities in end-stage renal failure with cardiac magnetic resonance imaging using native T1 mapping. *Kidney Int*. 2016;90(4):845-852. doi:10.1016/j.kint.2016.06.014
5. Romero-González G, González A, López B, Ravassa S, Díez J. Heart failure in chronic kidney disease: the emerging role of myocardial fibrosis. *Nephrol Dial Transplant*. 2020:1-8. doi:10.1093/ndt/gfaa284
6. Edwards NC, Moody WE, Yuan M, et al. Diffuse interstitial fibrosis and myocardial dysfunction in early chronic kidney disease. *Am J Cardiol*. 2015;115(9):1311-1317. doi:10.1016/j.amjcard.2015.02.015
7. Borrelli S, Provenzano M, Gagliardi I, et al. Sodium intake and chronic kidney disease. *Int J Mol Sci*. 2020;21(13):1-13. doi:10.3390/ijms21134744
8. Bottomley PA. Sodium MRI in human heart: A review. *NMR Biomed*. 2016;29(2):187-196. doi:10.1002/nbm.3265
9. Müller DN, Wilck N, Haase S, Kleinewietfeld M, Linker RA. Sodium in the microenvironment regulates immune responses and tissue homeostasis. *Nat Rev Immunol*. 2019;19(4):243-254. doi:10.1038/s41577-018-0113-4
10. Ouwerkerk R, Bottomley PA, Spooner AE, Tomaselli GF, Wu KC, Weiss RG. Tissue sodium concentration in myocardial infarction in humans. 2008;248(1).
11. Yu HCM, Burrell LM, Black MJ, et al. Salt induces myocardial and renal fibrosis in normotensive and hypertensive rats. *Circulation*. 1998;98(23):2621-2628. doi:10.1161/01.CIR.98.23.2621
12. Wallace M. Anatomy and Physiology of the Kidney. *AORN J*. 1998;68(5):799-820.
13. Qian Q. Salt, water and nephron: Mechanisms of action and link to hypertension and chronic kidney disease. *Nephrology*. 2018;23:44-49. doi:10.1111/nep.13465
14. Pettitt RM, Brumbaugh AP, Gartman MF, Jackson AM. Chronic kidney disease:

- Detection and evaluation. *Osteopath Fam Physician*. 2020;12(1):14-19. doi:10.33181/12011
15. Elliott DA. Hemodialysis. *Clin Tech Small Anim Pract*. 2000;15(3):136-148. doi:10.1053/svms.2000.18297
 16. Lee SW. Sodium balance in maintenance hemodialysis. *Electrolyte Blood Press*. 2012;10(1):1-6. doi:10.5049/EBP.2012.10.1.1
 17. Webster AC, Nagler E V., Morton RL, Masson P. Chronic Kidney Disease. *Lancet*. 2017;389(10075):1238-1252. doi:10.1016/S0140-6736(16)32064-5
 18. Kilmer PD. Hemodialysis. *Journalism*. 2010;11(3):369-373. doi:10.1177/1461444810365020
 19. Vadakedath S, Kandi V. Dialysis: A Review of the Mechanisms Underlying Complications in the Management of Chronic Renal Failure. *Cureus*. 2017;9(8). doi:10.7759/cureus.1603
 20. Shih HT. Anatomy of the action potential in the heart. *Texas Hear Inst J*. 1994;21(1):30-41.
 21. Liu M, Li XC, Lu L, et al. Cardiovascular disease and its relationship with chronic kidney disease. *Eur Rev Med Pharmacol Sci*. 2014;18(19):2918-2926.
 22. Carracedo J, Alique M, Vida C, et al. Mechanisms of Cardiovascular Disorders in Patients With Chronic Kidney Disease: A Process Related to Accelerated Senescence. *Front Cell Dev Biol*. 2020;8(March):1-14. doi:10.3389/fcell.2020.00185
 23. Sarnak MJ, Amann K, Bangalore S, et al. Chronic Kidney Disease and Coronary Artery Disease: JACC State-of-the-Art Review. *J Am Coll Cardiol*. 2019;74(14):1823-1838. doi:10.1016/j.jacc.2019.08.1017
 24. Sigrist M, Bungay P, Taal MW, McIntyre CW. Vascular calcification and cardiovascular function in chronic kidney disease. *Nephrol Dial Transplant*. 2006;21(3):707-714. doi:10.1093/ndt/gfi236
 25. McIntyre CW. The functional cardiovascular consequences of vascular calcification. *Semin Dial*. 2007;20(2):122-128. doi:10.1111/j.1525-139X.2007.00258.x
 26. Akchurin OM, Kaskel F. Update on inflammation in chronic kidney disease. *Blood Purif*. 2015;39(1-3):84-92. doi:10.1159/000368940
 27. Odudu A, McIntyre CW. An Update on Intradialytic Cardiac Dysfunction. *Semin Dial*. 2016;29(6):435-441. doi:10.1111/sdi.12532
 28. Slessarev M, Salerno F, Ball IM, McIntyre CW. Continuous renal replacement therapy is associated with acute cardiac stunning in critically ill patients. *Hemodial Int*. 2019;23(3):325-332. doi:10.1111/hdi.12760
 29. Penny JD, Grant C, Salerno F, et al. Percutaneous perfusion monitoring for the detection of hemodialysis induced cardiovascular injury. *Hemodial Int*. 2018;22(3):351-358. doi:10.1111/hdi.12632

30. Ahmadmehrabi S, Tang WHW. Hemodialysis-induced cardiovascular disease. *Semin Dial*. 2018;31(3):258-267. doi:10.1111/sdi.12694
31. Talman V, Ruskoaho H. Cardiac fibrosis in myocardial infarction—from repair and remodeling to regeneration. *Cell Tissue Res*. 2016;365(3):563-581. doi:10.1007/s00441-016-2431-9
32. Hinderer S, Schenke-Layland K. Cardiac fibrosis – A short review of causes and therapeutic strategies. *Adv Drug Deliv Rev*. 2019;146:77-82. doi:10.1016/j.addr.2019.05.011
33. González A, Schelbert EB, Díez J, Butler J. Myocardial Interstitial Fibrosis in Heart Failure: Biological and Translational Perspectives. *J Am Coll Cardiol*. 2018;71(15):1696-1706. doi:10.1016/j.jacc.2018.02.021
34. Mall G, Huther W, Schneider J, Lundin P, Ritz E. Diffuse Intermycardiocytic Fibrosis in Uraemic Patients. *Nephrol Dial Transplant*. 1990;5:39-44.
35. Graham-Brown MPM, March DS, Churchward DR, et al. Novel cardiac nuclear magnetic resonance method for noninvasive assessment of myocardial fibrosis in hemodialysis patients. *Kidney Int*. 2016;90(4):835-844. doi:10.1016/j.kint.2016.07.014
36. Hayer MK, Price AM, Liu B, et al. Diffuse Myocardial Interstitial Fibrosis and Dysfunction in Early Chronic Kidney Disease. *Am J Cardiol*. 2018;121(5):656-660. doi:10.1016/j.amjcard.2017.11.041
37. Beller G, Zaret B. Left Ventricular Hypertrophy. *Circulation*. 2000;101:1465-1478.
38. Lazzeroni D, Rimoldi O, Camici PG. From left ventricular hypertrophy to dysfunction and failure. *Circ J*. 2016;80(3):555-564. doi:10.1253/circj.CJ-16-0062
39. Kawel-Boehm N, Hetzel SJ, Ambale-Venkatesh B, et al. *Reference Ranges (“Normal Values”) for Cardiovascular Magnetic Resonance (CMR) in Adults and Children: 2020 Update*. Vol 22.; 2020. doi:10.1186/s12968-020-00683-3
40. Schneider MP, Raff U, Kopp C, et al. Skin sodium concentration correlates with left ventricular hypertrophy in CKD. *J Am Soc Nephrol*. 2017;28(6):1867-1876. doi:10.1681/ASN.2016060662
41. Bhawe G, Neilson EG. Body fluid dynamics: Back to the future. *J Am Soc Nephrol*. 2011;22(12):2166-2181. doi:10.1681/ASN.2011080865
42. Strazzullo P, Leclercq C. Nutrient Information.Sodium. *Adv Nutr*. 2014;2:188-190. doi:10.3945/an.113.005215.amount
43. Maudsley AA, Hilal SK. Biological aspects of sodium-23 imaging. *Br Med Bull*. 1984;40(2):165-166.
44. Sandstede JJW, Hillenbrand H, Beer M, et al. Time course of ²³Na signal intensity after myocardial infarction in humans. *Magn Reson Med*. 2004;52(3):545-551. doi:10.1002/mrm.20165
45. Madelin G, Lee JS, Regatte RR, Jerschow A. Sodium MRI: Methods and

- applications. *Prog Nucl Magn Reson Spectrosc.* 2014;79:14-47.
doi:10.1016/j.pnmrs.2014.02.001
46. Titze J, Lang R, Ilies C, et al. Osmotically inactive skin Na⁺ storage in rats. *Am J Physiol - Ren Physiol.* 2003;285(6 54-6):1108-1117.
doi:10.1152/ajprenal.00200.2003
 47. Titze J. Water-free sodium accumulation. *Semin Dial.* 2009;22(3):253-255.
doi:10.1111/j.1525-139X.2009.00569.x
 48. Hammon M, Grossmann S, Linz P, et al. ²³Na magnetic resonance imaging of the lower leg of acute heart failure patients during diuretic treatment. *PLoS One.* 2015;10(10):1-13. doi:10.1371/journal.pone.0141336
 49. Qirjazi E, Salerno FR, Akbari A, et al. Tissue sodium concentrations in chronic kidney disease and dialysis patients by lower leg sodium-²³ magnetic resonance imaging. *Nephrol Dial Transplant.* 2020:1-10. doi:10.1093/ndt/gfaa036
 50. Titze J, Shakibaei M, Schafflhuber M, et al. Glycosaminoglycan polymerization may enable osmotically inactive Na⁺ storage in the skin. *Am J Physiol - Hear Circ Physiol.* 2004;287(1 56-1):203-208. doi:10.1152/ajpheart.01237.2003
 51. Kopp C, Linz P, Dahlmann A, et al. ²³Na magnetic resonance imaging-determined tissue sodium in healthy subjects and hypertensive patients. *Hypertens (Dallas, Tex 1979).* 2013;61(3):635-640. doi:10.1161/HYPERTENSIONAHA.111.00566
 52. Lambie SH, Taal MW, Fluck RJ, McIntyre CW. Online conductivity monitoring: Validation and usefulness in a clinical trial of reduced dialysate conductivity. *ASAIO J.* 2005;51(1):70-76. doi:10.1097/01.MAT.0000150525.96413.AW
 53. Kim GH. Dialysis unphysiology and sodium balance. *Electrolyte Blood Press.* 2009;7(2):31-37. doi:10.5049/EBP.2009.7.2.31
 54. Francis S, Buchanan CE, Prestwich B, Taal MW. Sodium MRI: A new frontier in imaging in nephrology. *Curr Opin Nephrol Hypertens.* 2017;26(6):435-441.
doi:10.1097/MNH.0000000000000370
 55. McIntyre CW, Burton JO, Selby NM, et al. Hemodialysis-induced cardiac dysfunction is associated with an acute reduction in global and segmental myocardial blood flow. *Clin J Am Soc Nephrol.* 2008;3(1):19-26.
doi:10.2215/CJN.03170707
 56. Selby NM, McIntyre CW. The acute cardiac effects of dialysis. *Semin Dial.* 2007;20(3):220-228. doi:10.1111/j.1525-139X.2007.00281.x
 57. Pike MM, Luo CS, Clark MD, et al. NMR measurements of Na⁺ and cellular energy in ischemic rat heart: Role of Na⁺-H⁺ exchange. *Am J Physiol - Hear Circ Physiol.* 1993;265(6 34-6). doi:10.1152/ajpheart.1993.265.6.h2017
 58. Van Echteld CJA, Kirkels JH, Eijgelshoven MHJ, Van Der Meer P, Ruigrok TJC. Intracellular sodium during ischemia and calcium-free perfusion: A ²³Na NMR study. *J Mol Cell Cardiol.* 1991;23(3):297-307. doi:10.1016/0022-2828(91)90066-U

59. Pike MM, Kitakaze M, Marban E. ^{23}Na -NMR measurements of intracellular sodium in intact perfused ferret hearts during ischemia and reperfusion. *Am J Physiol - Hear Circ Physiol*. 1990;259(6 28-6). doi:10.1152/ajpheart.1990.259.6.h1767
60. Afsar B, Kuwabara M, Ortiz A, et al. Salt intake and immunity. *Hypertension*. 2018;72(1):19-23. doi:10.1161/HYPERTENSIONAHA.118.11128
61. Wilck N, Balogh A, Markó L, Bartolomeaus H, Müller DN. The role of sodium in modulating immune cell function. *Nat Rev Nephrol*. 2019;15(9):546-558. doi:10.1038/s41581-019-0167-y
62. Rossitto G, Delles C. Mechanisms of sodium-mediated injury in cardiovascular disease: old play, new scripts. *FEBS J*. 2021:1-14. doi:10.1111/febs.16155
63. Santoro A, Mancini E. Cardiac effects of chronic inflammation in dialysis patients. *Nephrol Dial Transplant*. 2002;17(SUPPL. 8):10-15. doi:10.1093/ndt/17.suppl_8.10
64. Beduschi GC, Telini LSR, Caramori JCT, Martin LC, Barretti P. Effect of dialysate sodium reduction on body water volume, blood pressure, and inflammatory markers in hemodialysis patients - A prospective randomized controlled study. *Ren Fail*. 2013;35(5):742-747. doi:10.3109/0886022X.2013.789961
65. Yamada T, Wakabayashi M, Bhalla A, et al. Cardiovascular and renal outcomes with SGLT-2 inhibitors versus GLP-1 receptor agonists in patients with type 2 diabetes mellitus and chronic kidney disease: a systematic review and network meta-analysis. *Cardiovasc Diabetol*. 2021;20(1):1-13. doi:10.1186/s12933-020-01197-z
66. Fernandez-Fernandez B, Sarafidis P, Kanbay M, et al. SGLT2 inhibitors for non-diabetic kidney disease: Drugs to treat CKD that also improve glycaemia. *Clin Kidney J*. 2020;13(5):728-733. doi:10.1093/CKJ/SFAA198
67. Lopaschuk GD, Verma S. Mechanisms of Cardiovascular Benefits of Sodium Glucose Co-Transporter 2 (SGLT2) Inhibitors: A State-of-the-Art Review. *JACC Basic to Transl Sci*. 2020;5(6):632-644. doi:10.1016/j.jacbts.2020.02.004
68. Cherney DZI, Verma S. DAPA-CKD: The Beginning of a New Era in Renal Protection. *JACC Basic to Transl Sci*. 2021;6(1):74-77. doi:10.1016/j.jacbts.2020.10.005
69. Pieske B, Maier LS, Piacentino V, Weisser J, Hasenfuss G, Houser S. Rate dependence of $[\text{Na}^+]_i$ and contractility in nonfailing and failing human myocardium. *Circulation*. 2002;106(4):447-453. doi:10.1161/01.CIR.0000023042.50192.F4
70. Luo M, Anderson ME. Mechanisms of altered Ca^{2+} handling in heart failure. *Circ Res*. 2013;113(6):690-708. doi:10.1161/CIRCRESAHA.113.301651
71. Lekawanvijit S. Cardiotoxicity of uremic toxins: A driver of cardiorenal syndrome. *Toxins (Basel)*. 2018;10(9). doi:10.3390/toxins10090352

72. Rossitto G, Touyz RM, Petrie MC, Delles C. Much ado about N . . . Atrium: Modelling tissue sodium as a highly sensitive marker of subclinical and localised oedema. *Clin Sci*. 2018;132:2609-2613. doi:10.1042/CS20190154
73. Rossitto G, Mary S, Chen JY, et al. Tissue sodium excess is not hypertonic and reflects extracellular volume expansion. *Nat Commun*. 2020;11(1):1-9. doi:10.1038/s41467-020-17820-2
74. Braam B, Lai CF, Abinader J, Bello AK. Extracellular fluid volume expansion, arterial stiffness and uncontrolled hypertension in patients with chronic kidney disease. *Nephrol Dial Transplant*. 2020;35(8):1393-1398. doi:10.1093/ndt/gfz020
75. Lemoine S, Salerno FR, Akbari A, McKelvie RS, McIntyre CW. Tissue Sodium Storage in Patients With Heart Failure: A New Therapeutic Target? *Circ Cardiovasc Imaging*. 2021;14(11):e012910. doi:10.1161/CIRCIMAGING.121.012910
76. Dahlmann A, Dörfelt K, Eicher F, et al. Magnetic resonance-determined sodium removal from tissue stores in hemodialysis patients. *Kidney Int*. 2015;87(2):434-441. doi:10.1038/ki.2014.269
77. Frohlich ED, Chien Y, Sesoko S, Pegram BL. Relationship between dietary sodium intake, hemodynamics, and cardiac mass in SHR and WKY rats. *Am J Physiol - Regul Integr Comp Physiol*. 1993;264(1 33-1). doi:10.1152/ajpregu.1993.264.1.r30
78. McRobbie DW, Moore EA, Graves MJ. *MRI from Picture to Proton*. 2nd ed. New York, NY: Cambridge University Press; 2006. doi:10.2214/ajr.182.3.1820592
79. Schulz-Menger J, Bluemke DA, Bremerich J, et al. Standardized image interpretation and post-processing in cardiovascular magnetic resonance - 2020 update: Society for Cardiovascular Magnetic Resonance (SCMR): Board of Trustees Task Force on Standardized Post-Processing. *J Cardiovasc Magn Reson*. 2020;22(1):1-19. doi:10.1186/s12968-020-00610-6
80. Konstandin S, Schad LR. Two-dimensional radial sodium heart MRI using variable-rate selective excitation and retrospective electrocardiogram gating with golden angle increments. *Magn Reson Med*. 2013;70(3):791-799. doi:10.1002/mrm.24523
81. Konstandin S, Nagel AM, Heiler PM, Schad LR. Two-dimensional radial acquisition technique with density adaption in sodium MRI. *Magn Reson Med*. 2011;65(4):1090-1096. doi:10.1002/mrm.22684
82. Hilal SK, Maudsley AA, Ra JB, et al. In vivo nmr imaging of sodium-23 in the human head. *J Comput Assist Tomogr*. 1985;9(1):1-7. doi:10.1097/00004728-198501000-00001
83. Zbýň Š, Mlynárik V, Juras V, Szomolanyi P, Trattnig S. Evaluation of cartilage repair and osteoarthritis with sodium MRI. *NMR Biomed*. 2016;29(2):206-215. doi:10.1002/nbm.3280
84. Christa M, Weng AM, Geier B, et al. Increased myocardial sodium signal intensity

- in Conn's syndrome detected by ^{23}Na magnetic resonance imaging. *Eur Heart J Cardiovasc Imaging*. 2019;20(3):263-270. doi:10.1093/ehjci/jej134
85. Ouwerkerk R, Weiss RG, Bottomley PA. Measuring human cardiac tissue sodium concentrations using surface coils, adiabatic excitation, and twisted projection imaging with minimal T2 losses. *J Magn Reson Imaging*. 2005;21(5):546-555. doi:10.1002/jmri.20322
 86. Lott J, Platt T, Niesporek SC, et al. Corrections of myocardial tissue sodium concentration measurements in human cardiac ^{23}Na MRI at 7 Tesla. *Magn Reson Med*. 2019;82(1):159-173. doi:10.1002/mrm.27703
 87. Axel L, Costantini J, Listerud J. Intensity Correction in Surface-Coil MR Imaging. *Am J Roentgenol*. 1987;148(February):418-420.
 88. Boehmert L, Kuehne A, Waiczies H, et al. Cardiorenal sodium MRI at 7.0 Tesla using a 4/4 channel $^1\text{H}/^{23}\text{Na}$ radiofrequency antenna array. *Magn Reson Med*. 2019;82(6):2343-2356. doi:10.1002/mrm.27880
 89. Resetar A, Hoffmann SH, Graessl A, et al. Retrospectively-gated CINE ^{23}Na imaging of the heart at 7.0Tesla using density-adapted 3D projection reconstruction. *Magn Reson Imaging*. 2015;33(9):1091-1097. doi:10.1016/j.mri.2015.06.012
 90. Graessl A, Ruehle A, Waiczies H, et al. Sodium MRI of the human heart at 7.0T: Preliminary results. *NMR Biomed*. 2015;28(8):967-975. doi:10.1002/nbm.3338
 91. Stocker D, Manoliu A, Becker AS, et al. Image Quality and Geometric Distortion of Modern Diffusion-Weighted Imaging Sequences in Magnetic Resonance Imaging of the Prostate. *Invest Radiol*. 2018;53(4):200-206. doi:10.1097/RLI.0000000000000429
 92. Ihalainen T, Sipilä O, Savolainen S. MRI quality control: Six imagers studied using eleven unified quality parameters. *Eur Radiol*. 2004;14(10):1859-1865. doi:10.1007/s00330-004-2278-4
 93. Qiu J, Wang G, Min J, Wang X, Wang P. Testing the quality of images for permanent magnet desktop MRI systems using specially designed phantoms. *Phys Med Biol*. 2013;58(24):8677-8687. doi:10.1088/0031-9155/58/24/8677
 94. Akbari A, Lemoine S, Salerno F, et al. Functional Sodium MRI Helps to Measure Corticomedullary Sodium Content in Normal and Diseased Human Kidneys. *Radiology*. 2022;(6). doi:10.1148/radiol.211238
 95. Salerno FR, Akbari A, Lemoine S, Scholl TJ, McIntyre CW, Filler G. Effects of pediatric chronic kidney disease and its etiology on tissue sodium concentration: a pilot study. *Pediatr Nephrol*. 2022. doi:10.1007/s00467-022-05600-7
 96. Qirjazi E, Salerno FR, Akbari A, et al. Tissue sodium concentrations in chronic kidney disease and dialysis patients by lower leg sodium- 23 magnetic resonance imaging. *Nephrol Dial Transplant*. 2021;36(7):1234-1243. doi:10.1093/ndt/gfaa036
 97. Bangarter NK, Kaggie JD, Taylor MD, Hadley JR. Sodium MRI radiofrequency

- coils for body imaging. *NMR Biomed.* 2016;29(2):107-118. doi:10.1002/nbm.3392
98. Giovannetti G, De Marchi D, Pingitore A. Radiofrequency coils and pulse sequences for cardiac magnetic resonance applications: New perspectives and future developments. *Rev Cardiovasc Med.* 2016;17(3-4):124-130. doi:10.3909/ricm0846
 99. Fessler JA. On NUFFT-based gridding for non-Cartesian MRI. *J Magn Reson.* 2007;188(2):191-195. doi:10.1016/j.jmr.2007.06.012
 100. Fedorov A, Beichel R, Kalpathy-Cramer J, et al. 3D Slicer as an Image Computing Platform for the Quantitative Imaging Network. *Magn Reson Imaging.* 2012;30(9):1323–1341. doi:10.1016/j.mri.2012.05.001
 101. Miller AJ, Joseph PM. The use of power images to perform quantitative analysis on low SNR MR images. *Magn Reson Imaging.* 1993;11(7):1051-1056. doi:10.1016/0730-725X(93)90225-3
 102. Ren H, Lin W, Ding X. Surface coil intensity correction in magnetic resonance imaging in spinal metastases. *Open Med.* 2017;12(1):138-143. doi:10.1515/med-2017-0021
 103. Insko EK, Clayton DB, Elliott MA. In vivo sodium MR imaging of the intervertebral disk at 4 T. *Acad Radiol.* 2002;9(7):800-804. doi:10.1016/S1076-6332(03)80350-1
 104. Lott J, Platt T, Niesporek SC, et al. Corrections of myocardial tissue sodium concentration measurements in human cardiac ²³Na MRI at 7 Tesla. *Magn Reson Med.* 2019;82(1):159-173. doi:10.1002/mrm.27703
 105. Ouwerkerk R, Weiss RG, Bottomley PA. Measuring human cardiac tissue sodium concentrations using surface coils, adiabatic excitation, and twisted projection imaging with minimal T2 losses. *J Magn Reson Imaging.* 2005;21(5):546-555. doi:10.1002/jmri.20322

Curriculum Vitae

Name:	Taylor Marcus
Post-secondary Education and Degrees:	<p>Master of Science Medical Biophysics The University of Western Ontario London, Ontario, Canada 2020-2022 (Expected)</p> <p>Bachelor of Medical Sciences Honours Specialization in Medical Biophysics (Medical Sciences Concentration) Western Scholars With Distinction The University of Western Ontario London, Ontario, Canada 2016-2020</p>
Honours and Awards:	<p>Province of Ontario Graduate Scholarship 2021-2022</p> <p>Indigenous Graduate Student Research Award 2021-2022</p> <p>Western Graduate Research Scholarship 2020-2022</p>
Related Experience	<p>Head & Heart Indigenous Research Fellowship The University of Western Ontario – Indigenous Initiatives 2022</p> <p>Graduate Students Association of Medical Biophysics The University of Western Ontario 2021-2022</p> <p>Academic Mentorship Program Executive Member – Medical Biophysics The University of Western Ontario 2021-2022</p>

Soup Kitchen Volunteer – Medical Biophysics Gives Back
The University of Western Ontario
2020-2022

Research Crowdfunding Campaign
Experiment.com
2020-2021

Publications:

Akbari A, Lemoine S, Salerno F, **Marcus TL**, Duffy T, Scholl TJ, Filler G, House AA, McIntyre CW. Functional Sodium MRI Helps to Measure Corticomedullary Sodium Content in Normal and Diseased Human Kidneys. *Radiology*. 2022 May;303(2):384-389.

Smith CW, **Marcus T**, Hoover D, Surry K, D'Souza D, Cool D, Kassam Z, Bastian-Jordan M, Gómez JA, Moussa M, Chin JL, Pautler S, Bauman GS, Ward AD. Targeting prostate lesions on multiparametric MRI with HDR brachytherapy: Optimal planning margins determined using whole-mount digital histology. *Brachytherapy*. 2022 Jul-Aug;21(4):435-441.